ELECTRICALLY CONTROLLED FRUSTRATION OF TOTAL INTERNAL REFLECTION ON TRANSPARENT SUPERHYDROPHOBIC SURFACES

by

STEVEN HAIPING GOU

B.Eng., McMaster University, 2007

A THESIS SUBMITTED IN PARTIAL FULFILLMENT OF
THE REQUIREMENTS FOR THE DEGREE OF

MASTER OF SCIENCE

in

THE FACULTY OF GRADUATE STUDIES

(Physics)

THE UNIVERSITY OF BRITISH COLUMBIA
(VANCOUVER)

NOVEMBER 2010

ABSTRACT

Superhydrophobic surfaces are those that have a very low adhesion to water due to a combination of surface chemistry and physical roughness. This low adhesion surface offers the potential for enabling low energy optical contact between a liquid and solid surface. For the purposes of this study, optical contact occurs when the distance between the liquid and solid surface is less than the evanescent wave region of light that is undergoing total internal reflection.

To develop an improved understanding of superhydrophobicity, a novel visualization technique was employed using neutrally buoyant immiscible liquids, which allowed liquid drops on the order of centimeters to be studied without distortion due to gravity. This allowed the visualization of wetting behaviors of liquids on different surface geometries, revealing the importance of overhanging structures to superhydrophobicity.

A nanoporous, optically transparent film of polymethyl-methacrylate (PMMA) was fabricated via oxygen plasma etching with roughness features on the order of 100 nm. The surface was made superhydrophobic by spin-coating with Teflon® AF.

A new technique was developed to modulate reflectivity by changing the optical properties at an interface by moving water to and from the interface. The technique electrically controls reflectance of visible light at a transparent superhydrophobic surface by frustration of total internal reflection and was demonstrated in an experimental device. The device consisted of a water drop positioned above a dual-scale superhydrophobic surface. Application of an electrical potential difference between the water and the surface caused it to undergo electrostatic deformation. This deformation would move the

water into optical contact with the transparent superhydrophobic surface, thereby changing the optical properties and enabling the modulation of the surface reflection. Removing the electrical potential caused the water to return to its original curvature, separating it from the superhydrophobic surface. Such a device has potential applications as a low-power reflective display.

The results presented in this work highlight the feasibility of this technique in practical devices, and suggest that further research is warranted.

TABLE OF CONTENTS

LIST OF TABLES

LIST OF FIGURES

ACKNOWLEDGEMENTS

I would like to thank all the members of SSP, both past and present. In particular, I would like to thank Peter Friedel, Weilai Li, Jason Radel, Allen Upward, Eri Watanabe, and Richard Wong, for their help and insights. Especially, I would like to thank Peter Hrudey for his help and guidance in the early stages of this research.

Special thanks to Andrzej Kotlicki for his advice and his incredible ability in procuring any piece of equipment imaginable.

I would like to thank all of the people at the various facilities involved in this research, including Eric La Fountaine, Douglas Justice, Derrick Horne, Brad Ross, Alina Kulpa, Mario Beaudoin, Mary Fletcher, Tom Cherng, Grace Li and Nathanael Sieb.

I am grateful for the financial and collaborative support provided by the 3M Company. In particular, I would like to thank John Huizanga for his valuable insights during discussions of various research problems.

Many thanks to my lab manager, Michele Mossman, whose contributions are far too numerous to list. Your help and dedication has helped make this lab a true joy to work in.

Sincere thanks to my research supervisor, Lorne Whitehead, for always being available with his timely guidance and for providing me with the freedom to explore. You have created a wonderful place to work that reflects your unique approach to research and I am grateful for everything I have learned from you.

Finally, thanks to Mom, Dad, and Lisa for your support in everything I do.

1 INTRODUCTION

Superhydrophobic surfaces are those in which surface chemistry and appropriate micro-scale and nano-scale geometries combine to produce materials with low adhesion to water. The phenomenon of superhydrophobicity can be found in nature[1], such as on the leaf of the euphorbia plant, pictured in Figure 1.1.Plants may have developed superhydrophobic properties for self-cleaning purposes, as water rolling off of a superhydrophobic surface carries with it loose particles that are on the surface.

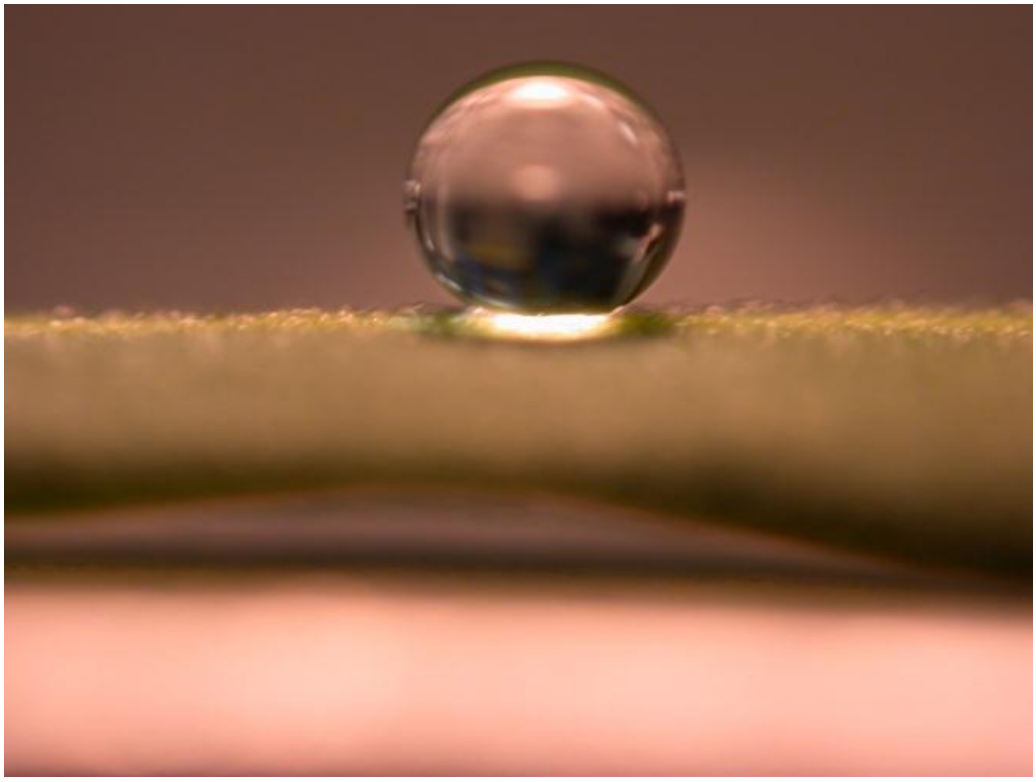

Figure 1.1: Photograph of water beading up on a plant leaf of the Euphorbia genus

Interest in superhydrophobic surfaces has increased in recent years in both science and industry. For example, the number of articles published on the subject from the years 2006 to 2007 was more than double the total number of publications up to that point on

superhydrophobicity[2]. Superhydrophobic materials have a wide variety of potential applications, such as self-cleaning surfaces, water repellant textiles, and anti-fogging coatings[3].

In the field of superhydrophobicity, there are some commonly held misconceptions[4]. These may have arisen from the governing equations of superhydrophobic surfaces, which are often applied without full understanding of their flaws[5]. In this work, a novel modeling technique involving neutrally buoyant immiscible liquids is presented. This approach provides large-scale visualization of wetting behavior without distortion from gravitational effects, and clearly illustrates the microscopic behavior of liquids on superhydrophobic surfaces.

The work presented in this thesis centers around a new technique which takes advantage of the low adhesion between water and superhydrophobic surfaces to reversibly change the reflectance at an optical interface. The technique was demonstrated experimentally in a prototype device and has potential applications in reflective display technology.

Reflective display technologies have recently become more prominent, especially in applications of portable electronics such as e-book readers. Reflective displays are able to electronically control the reflectance of light, creating images using reflected light from the ambient environment. These techniques are generally low in power, due to the lack of backlights, or internal light sources behind the screen image. They ideally produce high contrast images in direct sunlight, as well as under indoor lighting conditions.

The reversibly switchable reflective device demonstrated in this work relies on the phenomenon of frustrated total internal reflection. . The device consisted of a water drop above a superhydrophobic surface with two scales of roughness features; large-scale roughness features on the order of 100 μm, and on the surface between those structures, small-scale roughness features on the order of 100 nm. The small-scale superhydrophobic surface was optically transparent, while the large scale superhydrophobic structures were much larger than the evanescent region of totally internally reflected light. The movement of the water is used to controllably alter the optical properties at the interface.

Upon application of an electrical potential between the water drop and surface, the water underwent electrostatic deformation, flowed between the large structures, and made optical contact with the transparent surface by entering the evanescent region. As the size scale of

the roughness features on the transparent surface was on the order of the wavelength of visible light, a portion of light that normally underwent total internal reflection was coupled into the water, thereby reducing the intensity of the reflected light. Release of the electrical potential caused the water to return to its original shape. Due to the low energy of adhesion between the water and the transparent superhydrophobic surface, the water was able to separate from it. The energy of adhesion between water and smooth solid surfaces is prohibitively high, and release of water from the surface is only possible due to the low energy of adhesion between water and the superhydrophobic surface. The transparent superhydrophobic surfaces used in this study have a contact energy ten times less that of a smooth surface of the same material.

The phenomenon of frustrated total internal reflection is a familiar one in the field of optics, and can be found in fiber optic telecommunication systems in the form of unwanted crosstalk[7], and in optical equipment, such as beam splitters[8].

To lay the groundwork for the rest of this thesis, Chapter 2 reviews the background physics that is most relevant to this work.

In Chapter 3, a modeling technique for the wetting behavior of liquids on structured surfaces is presented. The technique takes advantage of immiscible, neutrally buoyant liquids to model on the macroscopic scale behavior of liquids on superhydrophobic surfaces at the microscopic scale. This technique was applied to the modeling of water drops under applied pressure on superhydrophobic surfaces consisting of features with two size scales. The modeling technique is quite versatile, providing insight into contact line movement and fluid deformation.

In Chapter 4, techniques for fabricating transparent superhydrophobic surfaces are discussed. Two coating techniques, octadecyltrimethoxysilane in solution and Teflon® AF[9] by spin coating, were used to alter the surface chemistry of samples. As well, two different techniques were examined to fabricate porous films with geometries suitable for superhydrophobicity. These were Glancing Angle Deposition[10] and plasma etch of polymethyl methacrylate (PMMA)[11]. A combination of Teflon® AF coating on plasma-etched PMMA was found to possess the properties desirable for applications in reversibly modulated reflectance devices. The angular dependence of reflected intensity of Teflon® AF-

coated plasma-etched PMMA films was simulated by approximating the porous film as optically homogenous films with effective refractive indices corresponding to the fractional volume of PMMA and air in the porous film. The force of adhesion of the transparent superhydrophobic surfaces was calculated based on contact angles and was experimentally measured.

In Chapter 5, a device that demonstrated electrical control of frustrated total internal reflection is presented. The device structure, relevant design details and experimental setup used to test the devices are discussed. Finally, the chapter culminates in experimental data of a working demonstration of a device that was capable of multiple, reversible changes in optical reflectance. The time required for the change in reflectance in response to an applied electrical potential is found to be in the range of 1 to 10 ms, depending on initial conditions. This is quite fast for a variably reflective display.

Chapter 6 presents the conclusions from this work. The results suggest that potential applications such as reflective displays are feasible. Finally, suggested future research into these topics are outlined.

2 BACKGROUND

This study incorporates ideas from a number of different fields. Thus, it is useful to provide a brief overview of the physical principles most relevant to the work presented in this thesis.

2.1 Total Internal Reflection

The index of refraction, *n*, of a material is the ratio of the speed of light in the material, *v*, to the speed of light in vacuum, c, as shown in Equation (1).

$$n = {}^{c}/_{v} \tag{1}$$

When light reaches an interface between optically transparent materials of two different refractive indices, a fraction of light is reflected and the remaining light is transmitted. The reflected light travels at an angle equal to the incident angle, while the transmitted light that passes from a material of index of refraction n_1 to a material of index of refraction n_2 behaves according to the relationship in Equation (2).

$$n_1 \sin\theta_1 = n_2 \sin\theta_2 \tag{2}$$

θ_1 is the incident angle and θ_2 is the transmitted angle as measured from the normal of the interface, illustrated in Figure 2-1(a). The relationship in Equation (2) is called Snell's law.

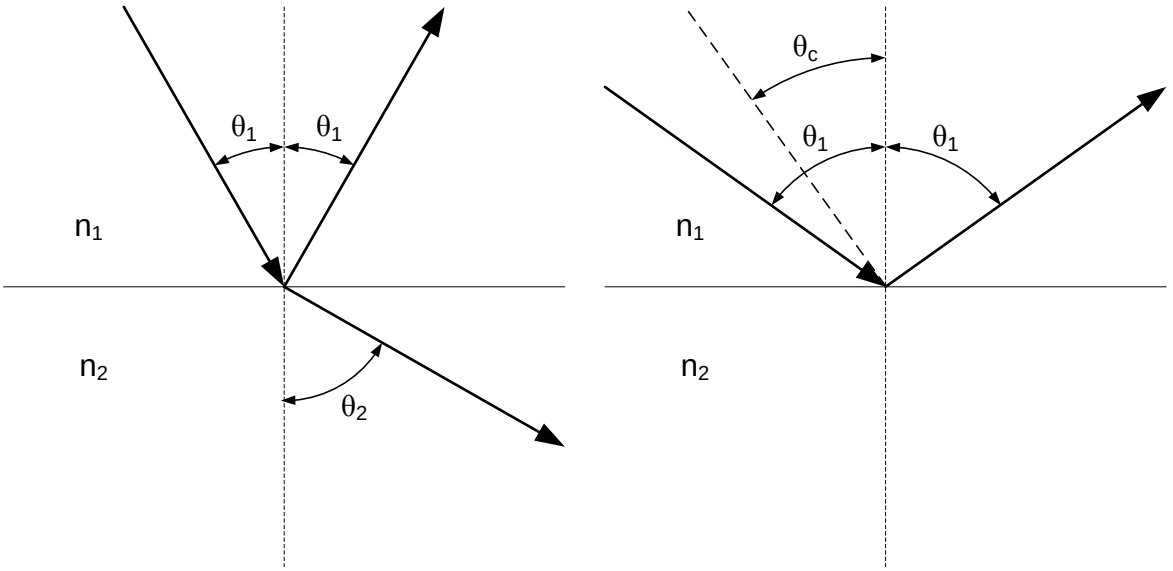

(a) (b)

Figure 2.1: a) Snell's Law b) Reflection past critical angle

In the case where light travels from a higher index material to a lower index material, the solution to the transmitted angle, θ_2, becomes a complex solution when θ_1 is greater than what is called the critical angle, θ_c (Figure 2.1(b)). The critical angle is found using Snell's law when θ_2 equals 90°, shown in Equation (3).

$$\theta_c = \sin^{-1}(n_2/n_1) \tag{3}$$

Beyond critical angle, all of the incident light reflects at the interface and no portion of the light is transmitted into the second medium (Figure 2.1(b)). This phenomenon is called total internal reflection (TIR). Some energy does penetrate a short distance into the second medium, and is termed the evanescent wave. Conservation of energy is not violated as this evanescent wave does not transmit through the second medium, but rather, this energy circulates back and forth between the two media, resulting in no net transfer of energy into the second medium. The evanescent wave propagates in a direction parallel to the interface as shown in Figure 2.2(a). The amplitude of the evanescent wave decreases exponentially with distance into the second medium, and for light of wavelength λ incident on the interface at angle θ, is characterized by the penetration depth[12] δ in Equation (4).

$$\delta = \frac{\lambda}{2\pi\sqrt{(sin^2\theta/n^2)-1}} \quad (4)$$

At a distance δ from the interface, the amplitude of the evanescent wave decreases by a factor of 1/e. Under normal circumstances, the energy in this wave returns to medium 1. However, if a third medium of index of refraction higher than medium 2 enters the evanescent wave region, as shown in Figure 2.2(b), than the evanescent wave energy can be coupled into medium 3 and the reflected intensity is reduced. This phenomenon is known as frustrated total internal reflection.

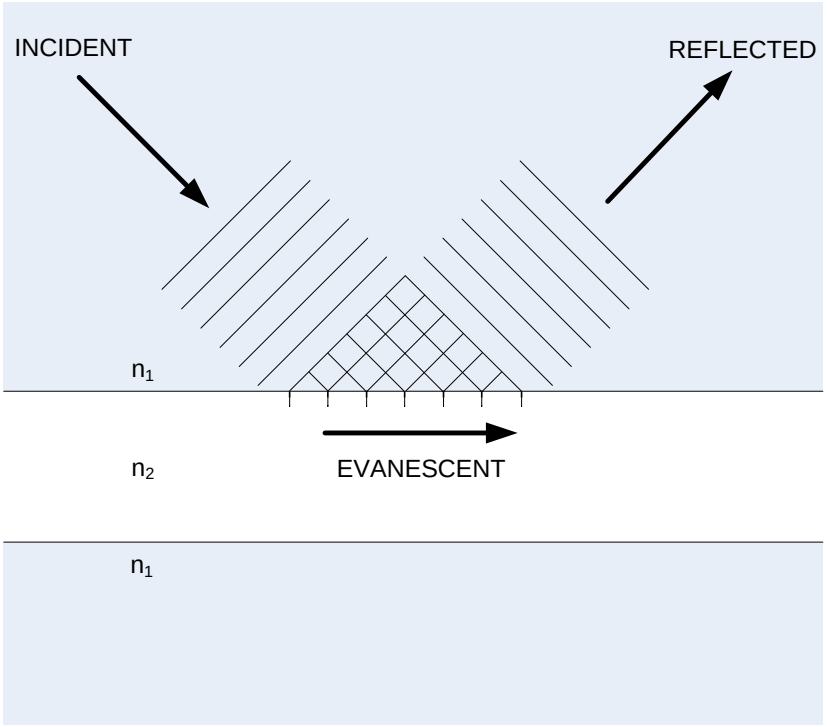

(a)

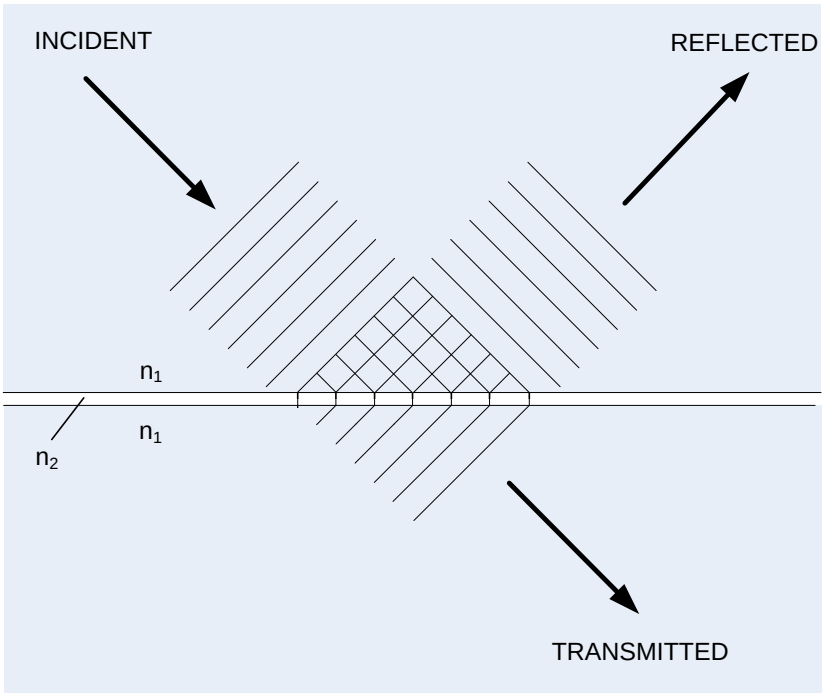

(b)

Figure 2.2: a) Total internal reflection of light incident on an interface and b) total internal reflection frustrated by third medium

2.2 Surface Tension and Contact Angle

2.2.1 Surface Tension and Surface Energy

Surface energy is the energy per unit area of the interface between two different substances. Surface energy, γ, is a scalar that has units of J/m^2 and is the quantification of the work required to create more surface area between two substances. Surface tension has units of N/m, which is numerically equivalent to surface energy and describes the same phenomenon. However, there are subtle conceptual differences between the two. Surface tension is a vector quantity that acts perpendicularly to a line on the surface.

Surface tension results from the minimization of free energy, one such form being the intermolecular attractions in a material. Molecules in the bulk of a material experience attractive forces equally in all directions. However, molecules at an interface are not surrounded by like molecules, and so experience a net force.

In a three phase system, such as that of a liquid drop resting on a solid surface in a vapor environment, the surface tensions between the three interfaces determines the angle that the liquid makes with the solid surface. This is termed the contact angle.

2.2.2 Contact Angle

Contact angle is a measure of the contact energy of a liquid on a solid surface. Consider the case of a liquid drop resting on a planar solid surface in a gaseous environment. If the liquid drop is small enough for gravitational effects to be negligible, the drop will form the shape of a sphere section truncated at the solid surface. Contact angle, θ_c, is defined as the angle the liquid makes with the solid surface as measured from the inside of the liquid drop as shown in Figure 2.3. The solid-vapor interfacial tension, γ_{sv}, the solid-liquid interfacial tension, γ_{sl}, and the liquid-vapor interfacial tension γ, are forces that act in a direction perpendicular to a line on their respective interfaces. At the three phase contact line, these forces act in the directions shown in Figure 2.3. The contact angle can simply be found by the balance of the

horizontal components of these forces at the three phase contact line and the resulting equation is known as Young's equation, Equation (5).

$$\gamma_{sv} = \gamma_{sl} + \gamma\cos\theta_c \tag{5}$$

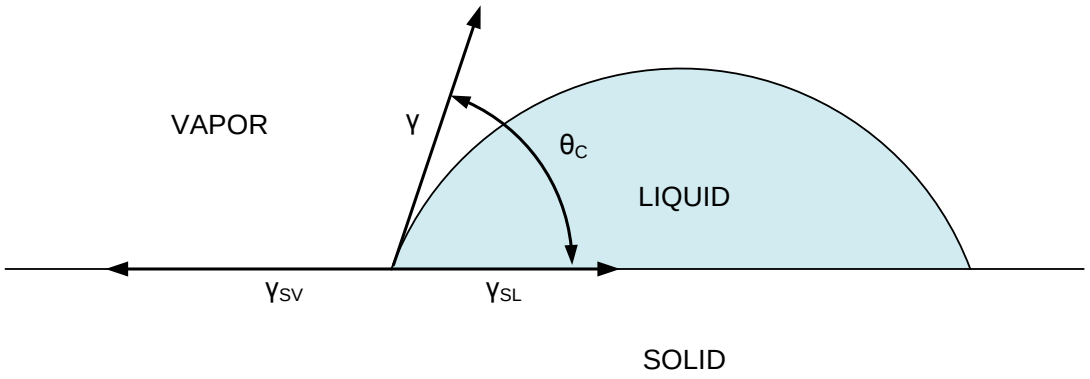

Figure 2.3: Balance of surface tension forces that lead to contact angle

In reality, the contact angle depends on the direction of motion of the contact line. If a liquid drop moves down a sloped surface, as in Figure 2.4, the advancing contact angle is the angle formed by the leading edge of the drop, and the receding contact angle is the angle formed by the trailing edge. The difference between the advancing and receding angles is termed the contact angle hysteresis, and is a measure of irreversible processes involved in the adhesion of the surface caused by surface roughness and chemical inhomogeneity.

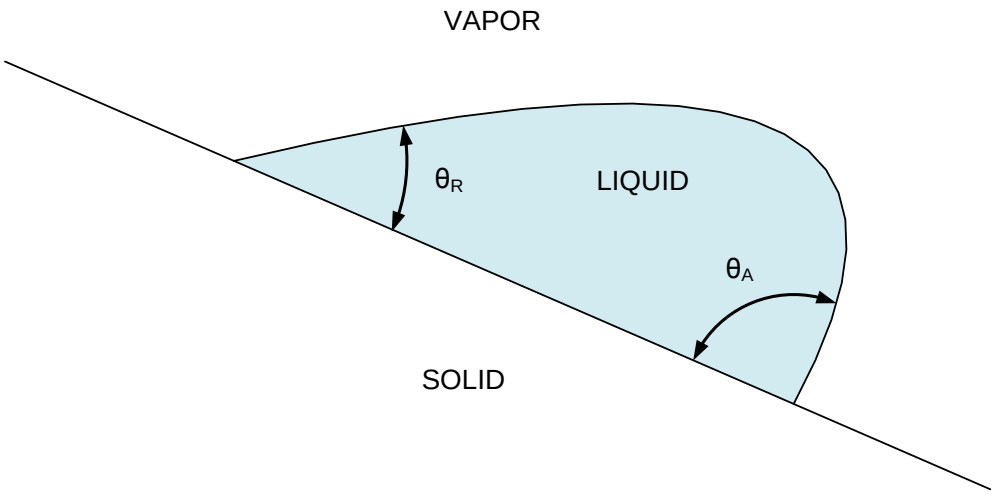

Figure 2.4: Advancing and receding contact angles of a liquid drop on an inclined plane

Up until now, this overview has focused on smooth solid surfaces. The wetting properties of a surface can also be affected by introducing surface roughness, as discussed in the next section.

2.3 Superhydrophobicity

2.3.1 Wenzel and Cassie-Baxter Models

The contact angle between a solid surface and a liquid is an intrinsic property of the surface chemistry. However, wettability of the surface can also be modified by surface geometry. When a solid surface is roughened, the apparent contact angle of a liquid drop can be estimated using one of two models: Wenzel[13] and Cassie-Baxter[14]. The apparent contact angle is the contact angle as measured from a straight horizontal line drawn across the top of the roughness geometries of a surface. As a general rule of thumb, a surface is considered superhydrophobic if the apparent contact angle between the water and surface is greater than 150^{o} [15].

Before proceeding, it is important to stress that the Wenzel and Cassie-Baxter equations are not laws, but simply observations that are valid under certain circumstances. These equations do not describe the underlying physics of the wetting behavior of liquids on a structured surface, which is discussed in detail in Chapter 3.

Wenzel[16] described the case wherein a roughened surface is fully wetted by the liquid as illustrated in Figure 2.5(a). The equation for the apparent contact angle in this case is shown in Equation (6).

$$\cos\theta_{rough} = r\cos\theta_{flat} \tag{6}$$

where r is the roughness factor defined as the ratio of the actual surface area of the roughened surface to the projected planar area and θ_{flat} is the contact angle as calculated from Equation (5) for a smooth surface. This equation is a simple modification of the Young equation and simply states that if the roughness factor is two, than the roughened surface is equivalent to that of a smooth surface with an interfacial surface energy which is double it. For a smooth surface, r=1 and the equation simplifies to the Young equation.

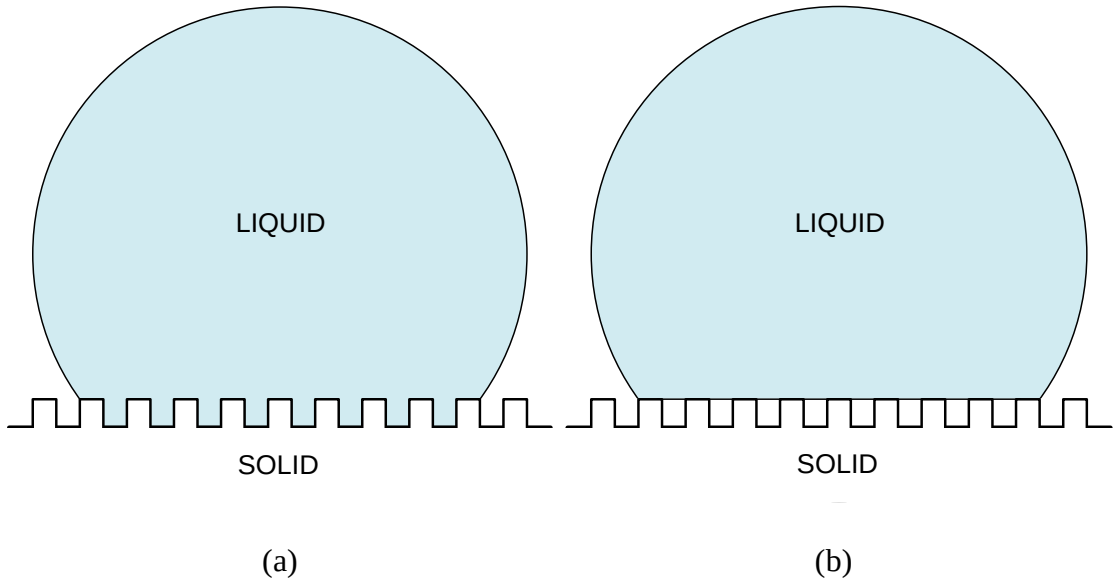

Figure 2.5: Liquid drop in a) Wenzel state and b) Cassie-Baxter state

Cassie and Baxter[17] described the case of a roughened surface which is not fully wetted, as illustrated in Figure 2.5(b). Their equation, (7), describes a liquid drop sitting on top of the surface features of a porous surface with air trapped underneath.

$$\cos\theta_{rough} = f\cos\theta_{flat} + f - 1 \tag{7}$$

where *f* is the fractional area of the solid surface defined in Equation (8).

$$f = \frac{\sum a}{\sum(a+b)} \tag{8}$$

The parameter, *a*, is the total area of solid on the porous surface and *b* is the area of air. In other words, *f* is simply the ratio of the solid surface area to the total surface area. Equation (7) comes from energy considerations. In essence, the Cassie-Baxter equation replaces the interfacial surface energy between the liquid-solid interface with a combination of the surface energy of the liquid-solid interface and the surface energy of the liquid-air interface in the ratios of their respective fractional areas on the porous surface.

In the case of the Wenzel state, increased roughness acts to increase the total force of adhesion. This is because for a fully wetted surface, increasing roughness increases the total area in contact between the liquid and solid surfaces. This is not so in the Cassie-Baxter case, where increasing roughness can actually decrease the total liquid-surface contact area, resulting in surfaces with a much lower force of adhesion to liquid than that of a smooth surface of the same material.

A liquid drop can transition between the Cassie-Baxter state to the Wenzel state if sufficient pressure is applied to the liquid. This is a common mode of failure for superhydrophobic surfaces, as the liquid becomes trapped in the pores and wets the surface.

2.3.2 Fluid Deformation under Applied Pressure

The pressure difference between two fluid regions separated by an interface is dependent on the principal radii of curvature, r_1 and r_2. For any point on a surface, the two principal radii of curvature of the surface are those that are on planes perpendicular to each other, and

intersect each other along the normal of the surface. The difference in pressure between the two fluids is given by the Young-Laplace equation, (9).

$$\Delta P = {}^{\gamma}/_{r_1} + {}^{\gamma}/_{r_2} \tag{9}$$

In the axisymmetric case where the radii of curvature are equal, this simplifies to Equation (10).

$$\Delta P = \frac{2\gamma}{r} \tag{10}$$

If the pressure difference is zero, the radii of curvature become infinite. That is to say, the interface between the two fluid regions of equal pressure is a flat plane. If one of the liquids is subjected to an applied pressure, then the radii of curvature will decrease according to (10). The applied pressure could be in the form of electrostatic pressure. Electrostatic pressure occurs when an electrical potential difference is applied between two conductors. The resulting charge accumulation at the surface of the two conductors results in an attractive force. If one of the conductors is a liquid, this charge accumulation will cause the liquid to deform towards the other conductor. In the case of an applied electrical potential between a conductive fluid and a conductive plane, as a first approximation, the electrostatic pressure can be expressed as that between two parallel planes, as shown by Equation (11).

$$P = \frac{\epsilon_0 V^2}{2d^2} \tag{11}$$

where V is the applied potential and d is the distance between the fluid and conductive plane. Upon application of this electrostatic pressure, the fluid will deform such that the Young-Laplace pressure, Equation (9), equals the electrostatic pressure.

2.3.3 Overhang

The Wenzel and Cassie-Baxter equations are useful approximations for superhydrophobic surfaces. However, they are an incomplete description of superhydrophobicity and should be used with understanding of their limitations when dealing with complex surface geometries. One such geometry is overhanging structures, or projections which jut out and over the surface, which enhances the robustness of superhydrophobic surfaces.

The importance of overhanging structures was illustrated by Ahuja et al[18]. They designed a nanonail geometry (Figure 2.6) which resists wetting of the surface. This resistance to wetting becomes apparent when comparing the behavior of liquids on the nanonail surface under applied pressure with that of a structured surface with no overhanging features.

In the case of vertical post geometries with no overhanging structures, the film will become fully wetted once the pressure applied overcomes the capillary pressure[19]. Capillary action occurs in thin tubes or pores and is a result of the forces of attraction between a liquid and the solid material of the tube. If the contact angle between the liquid and solid is less than 90º, than the liquid will have a tendency to wet into the tube. If the contact angle is greater than 90º, than the liquid will resist wetting into the tube, and a pressure, termed the capillary pressure, must be applied to the liquid to cause it to wet the tube. Contact angles greater than 90º is required to produce superhydrophobicity on structured surfaces with no overhanging features.

In the case of the nanonail geometry, as pressure is applied to the liquid, the contact line will move to the bottom of the nanonail head and become pinned to the underside of the nails. The contact line of the liquid will not be able to move until the pressure is increased such that that the contact angle between the liquid and the surface of the underside of nanonail head equals the advancing contact angle. Thus, a large pressure is required for the liquid to wet the bottom of each nail head.

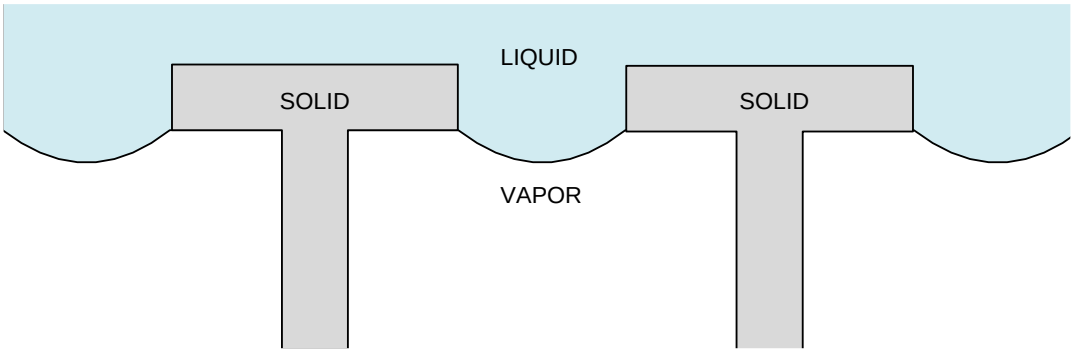

Figure 2.6: Liquid resting on nanonail structures

It is illustrative to compare the difference in pressures required to wet a vertical-walled geometry and one with overhang. For a vertical-walled, cylindrically symmetric geometry, liquid will wet into the pores if the capillary pressure, given by Equation (12), is surpassed:

$$P = \frac{2\gamma cos\theta}{a} \tag{12}$$

where a is the radius of the opening and θ is the intrinsic contact angle between the liquid and the surface. For simplicity, we will assume the 1 dimensional case, as illustrated in Figure 2.7(a), and so the capillary pressure simply becomes Equation (13).

$$P = \frac{\gamma cos\theta}{a} \tag{13}$$

For overhanging structures, the pressure must be large enough to produce a curvature large enough that the liquid wets the bottom of the surface as calculated by the Young-Laplace equation, (10). For the dimensions illustrated in Figure 2.7(b), this occurs when the radius of curvature equals a. Thus, the pressure required to wet into the overhang structure is given by Equation (14).

$$P = \frac{\gamma}{a} \tag{14}$$

This is an improvement of a factor of $1/cos\theta$ compared to that of the vertical wall structures.

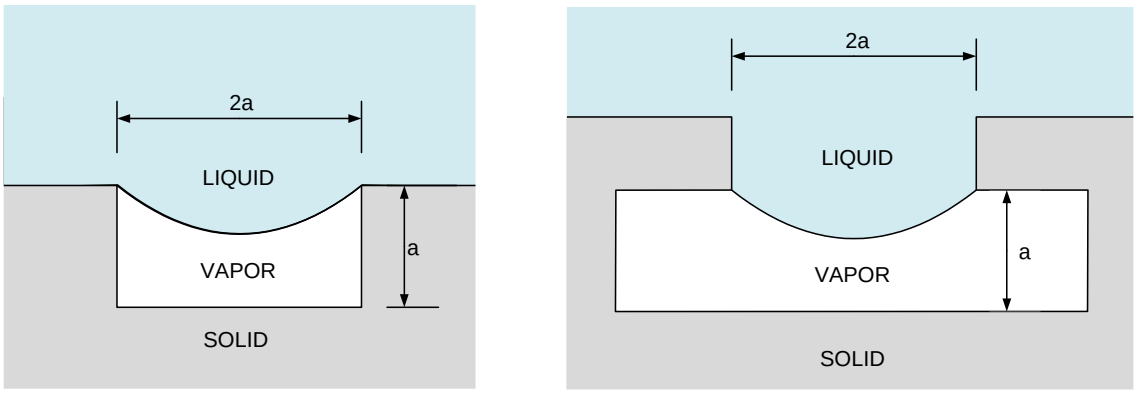

(a) (b)

Figure 2.7: Wetting behavior of a) a vertical walled structure and b) overhang structure

A second advantage of overhang is the possibility of superhydrophobic surfaces on materials with intrinsic contact angles less than 90°. This is not possible with vertical post structures because for intrinsic contact angles less than 90°, the capillary pressure changes sign, and the liquid will spontaneously wet into the pores without any applied pressure.

An alternative geometry to nanonails that also provides overhanging features is a surface covered with spheres. The bottom half of each sphere provides an overhanging structure, similar to the underside of a nanonail head. Sphere-covered surfaces are discussed in greater detail in Chapter 3.

2.3.4 Dual Scale Roughness

Another complexity that the Wenzel and Cassie-Baxter equations do not completely describe are superhydrophobic surfaces made of multiple-scale roughness features. On a surface with dual-scale roughness, the small-scale roughness features on the sides of large-scale structures can simply be viewed as multiple, small overhanging structures and provides the same advantages that large overhanging structures do, as illustrated in Figure 2.8.

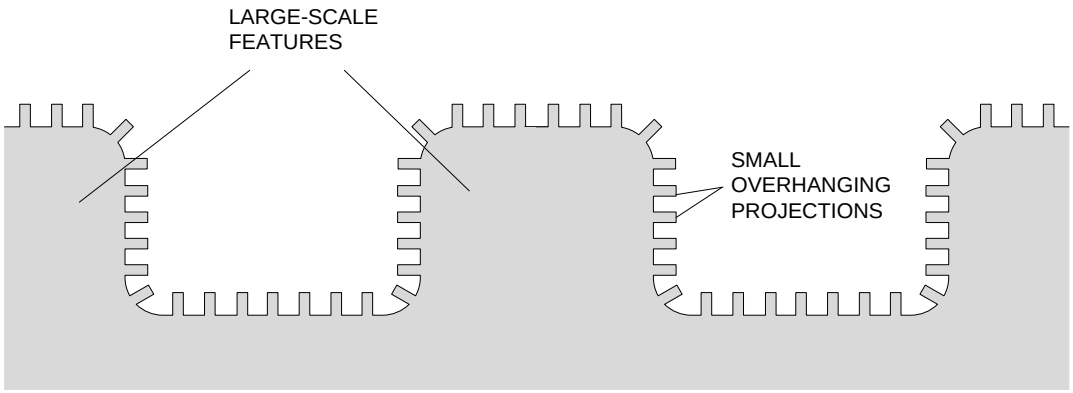

Figure 2.8: Superhydrophobic surface with dual-scale roughness

A second advantage of dual-scale roughness was discussed in a study of superhydrophobic plant leaves[20]. In it, the authors observed that many superhydrophobic plants have a large-scale geometry coated with a smaller-scale roughness in the form of micrometer-size wax crystals. This can be seen on the leaves of the euphorbia plant. Imaging by environmental scanning electron microscopy (ESEM) (Figure 2.9) clearly shows two scales of roughness on the euphorbia leaf surface. The authors suggest that this dual-scale roughness protects the smaller-scale roughness against abrasion. Although the wax crystals on the tops of the large structures are easily damaged, the crystals nestled between the large-scale surface features remain intact, and preserve the superhydrophobic nature of the leaf.

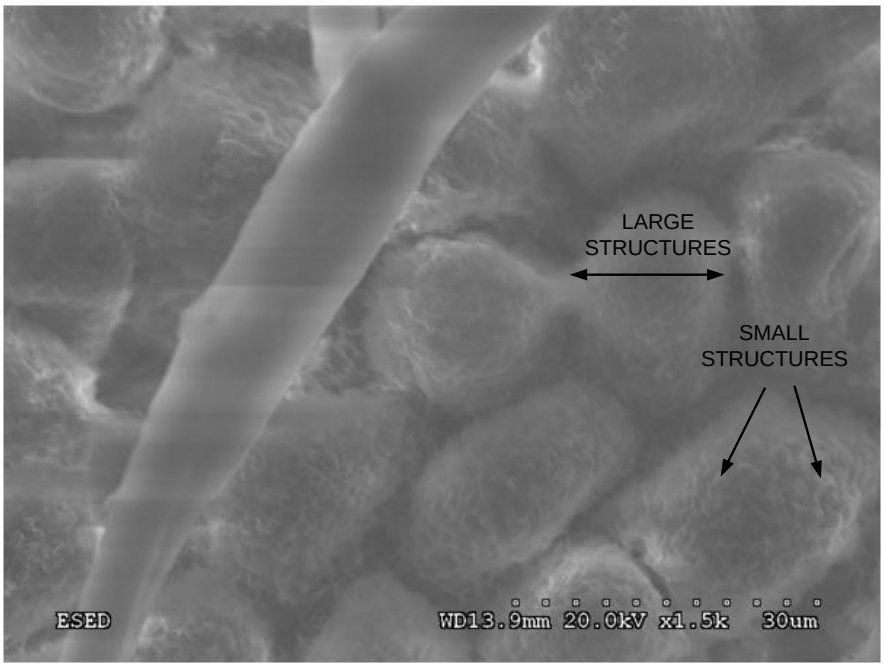

Figure 2.9: ESEM Image of Euphorbia leaf surface at 1500x magnification

3 NEUTRAL BUOYANCY MODELING

3.1 Problems with Wenzel and Cassie-Baxter Models

The Wenzel and Cassie-Baxter equations for apparent contact angles on roughened surfaces are widely used on superhydrophobic materials. However, these equations are approximations and should be used with an understanding of their limitations. Misunderstanding related to these equations can be partly attributed to the belief that the Wenzel and Cassie-Baxter equations are laws, when this is simply not the case[21]. There are several articles detailing the flaws of these equations, most notably by Gao and McCarthy[22,23,24,25]. This will not be discussed in detail here, but a simple example, which has been demonstrated experimentally by Gao and McCarthy[26], should convince the reader that the Wenzel and Cassie-Baxter equations are not fundamental laws, as some have erroneously claimed[27,28].

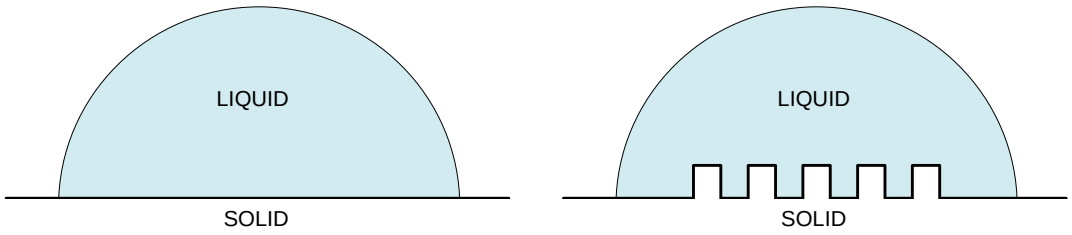

Figure 3.1: a) Liquid drop on a smooth solid surface b) Liquid drop on a surface with roughness far from the 3 phase contact line

Consider a liquid drop on a smooth surface as depicted in Figure 3.1(a). The contact angle that the liquid makes with the surface is determined by Young's equation, (5). If roughness is introduced to the solid surface inside the liquid contact area (Figure 3.1(b)) but away from the contact perimeter, then both the Wenzel and Cassie-Baxter equations would predict that the contact angle of the liquid drop would change. This was proven to be incorrect by Gao

and McCarthy through experiment[29]. The three phase contact line where the contact angle is measured cannot be affected by surface features far from it.

3.2 Neutral Buoyancy Visualization Technique

This experiment highlights the point that the fundamental behavior which determines a surface's wetting is solely determined by the three-phase contact line that the liquid makes with a solid surface.

To illustrate this point, a novel modeling technique is presented in order to visually represent the interactions that occur on superhydrophobic surfaces at the microscopic scale. Two immiscible, neutrally buoyant fluids, namely mineral oil and a water-ethanol mixture, were used in this experiment. Neutral buoyancy allows the use of centimeter-sized liquid drops. Gravity would otherwise cause an unacceptable degree of distortion of such large drops. The solid surfaces were coated with Teflon® AF to ensure that the intrinsic contact angle between the liquid drop and solid were the same for each of the different geometries that were used.

3.3 Modeling of a Flat Surface and Sphere-Covered Surface

In this experiment, the different behaviors of a liquid drop on a smooth surface and on a superhydrophobic surface covered by an array of spheres positioned in a square grid pattern were compared.

Figure 3.2 shows a water-ethanol drop in a mineral oil environment was placed on a solid Teflon® AF coated surface. The neutral buoyancy technique modeled a liquid drop that had formed a truncated sphere section and found its contact angle of 105±1º on a smooth surface.

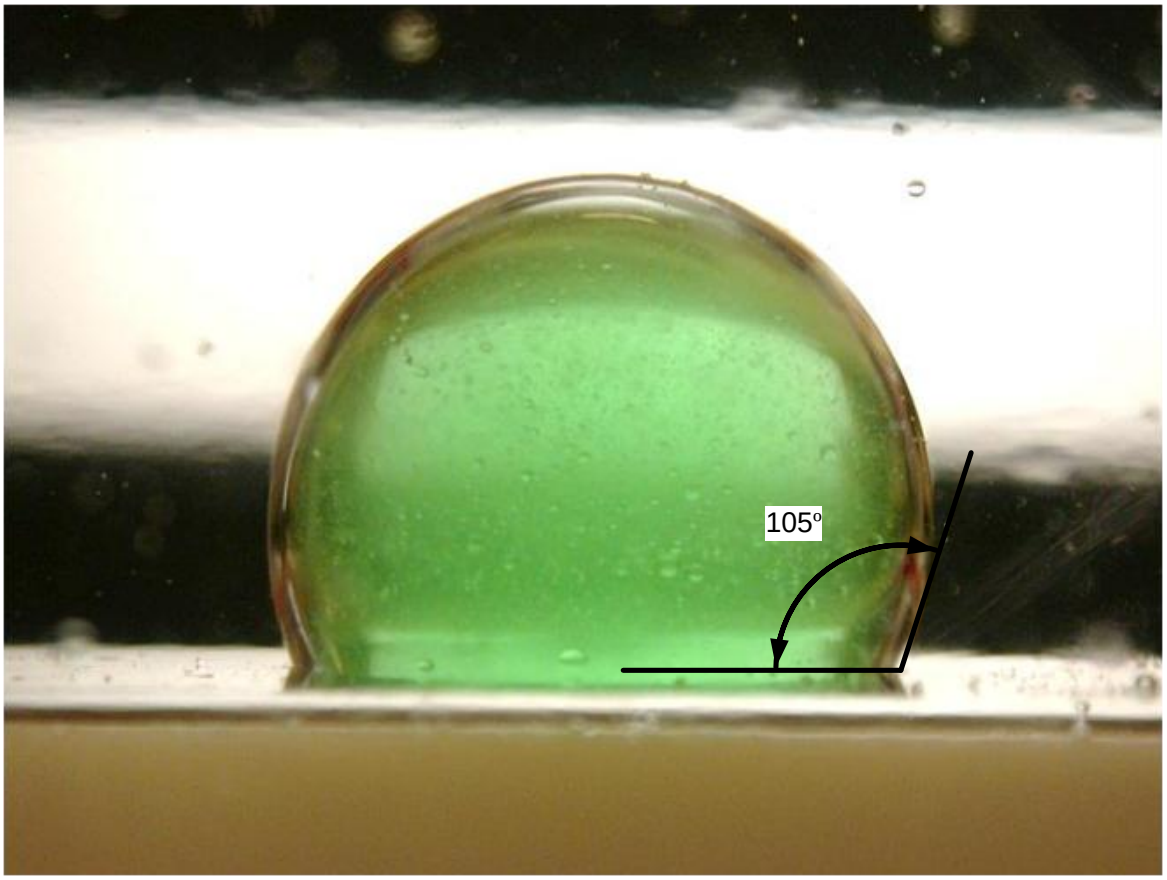

Figure 3.2: Photograph of the neutral buoyancy experiment modeling a drop on a smooth surface. The water-ethanol drop is surrounded by mineral oil. The drop is colored green using water-soluble dye for ease of visualization. The size of the water-ethanol drop is approximately 8 cm across.

Figure 3.3 shows the neutral buoyancy modeling technique applied to a liquid drop on a superhydrophobic surface. This particular superhydrophobic surface was one covered by equally-spaced spheres arranged in a square array. The liquid drop is shown to have a much larger apparent contact angle, 150±1º, than that of the smooth surface. This apparent contact angle comes about because of the intrinsic contact angle that the liquid drop makes with the surface features, as depicted in Figure 3.3. The experiment clearly shows that the contact angle between the liquid and the surface features is equal to that of the contact angle on a smooth surface, 105±1°. The combination of this intrinsic contact angle and the features touching the edge of the drop determines the apparent contact angle of structured surfaces.

This is in contrast with the Wenzel and Cassie-Baxter equations, since both of those equations predict that roughness features far from the liquid drop perimeter would have an effect on the apparent contact angle at the drop perimeter. Figure 3.3 shows that this is not the case.

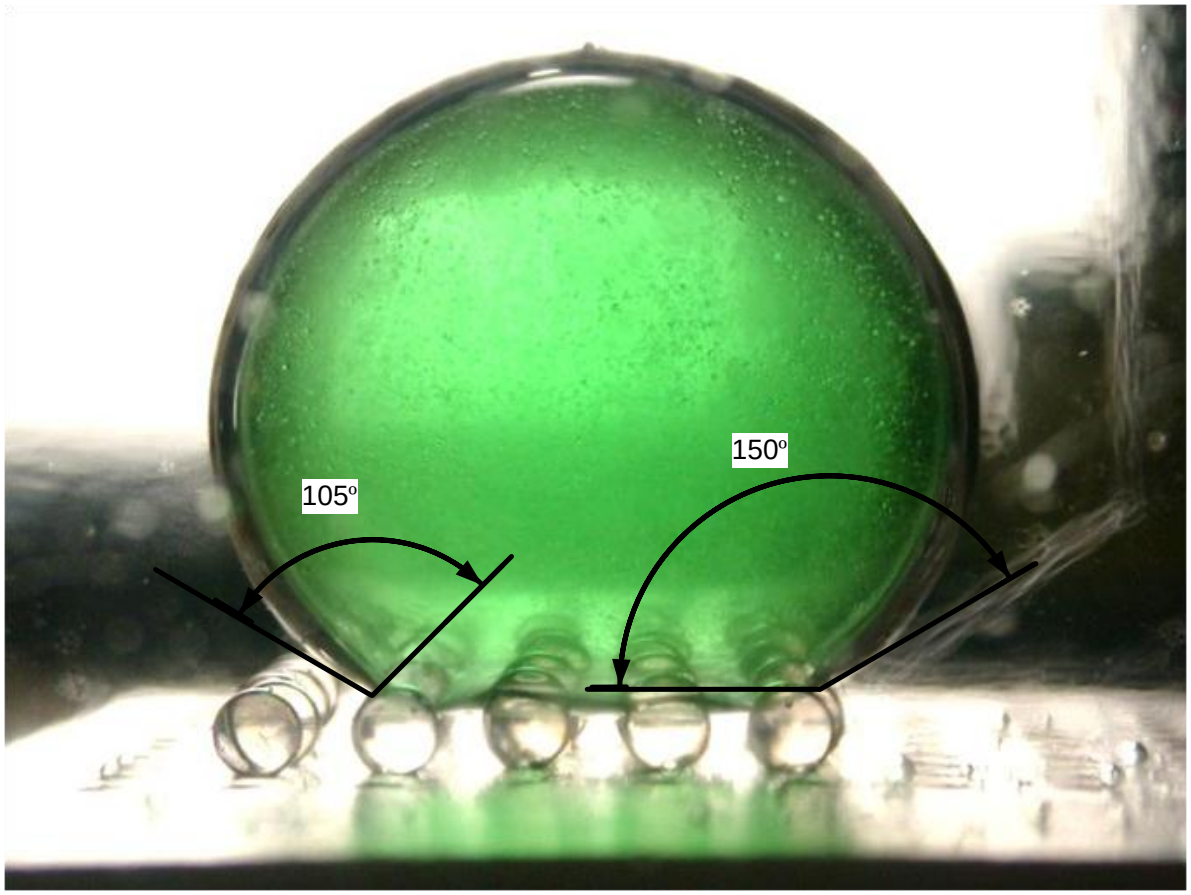

Figure 3.3: Neutral buoyancy experiment simulating a drop on a surface covered by spheres arranged in a square array. The diameter of the drop is approximately 8 cm. The apparent contact angle is measured to be 150º while the local contact angle at the sphere surface is measured to be 105º.

The neutral buoyancy modeling technique can be applied to surfaces with more complex surface geometries, as well as to systems having dynamically changing conditions such as pressure and contact line movement.

3.4 Modeling of a Dual-Scaled Superhydrophobic Surface with Applied Pressure

The neutral buoyancy method was also used to illustrate the working principal of frustration of total internal reflection on a superhydrophobic surface by deformation of a liquid, which forms the basis of the optical device presented in Chapter 5. Figure 3.4 shows the behavior of a liquid drop on a dual-scaled superhydrophobic surface as it underwent a varying, applied pressure. The dual-scaled superhydrophobic surface consisted of large-scale features with small-scale features on the surface between them. In this neutral buoyancy experiment, the large-scale features were 6.35 mm diameter spheres and the small-scale features were 0.635mm diameter spheres. This experiment represents a 6000:1 increase in scale, meaning that the large-scale spheres represented micrometer-scale roughness features while the smaller spheres represented roughness features on a transparent superhydrophobic surface with feature sizes on the order of 100 nm.

In Figure 3.4(a), the drop rested on the large-scale structures, maintaining the liquid well above the small-scale surface features, so that no optical contact is made. In Figure 3.4(b), a physical pressure was applied by pressing down on the liquid drop with a Teflon® block, causing the drop to undergo deformation and decrease its radius of curvature. Teflon® was used in this way because the energy of adhesion between the water-ethanol mixture and Teflon® was very small compared to that between mineral oil and Teflon®, so that the water-ethanol drop did not wet the Teflon® block. Thus, pressure could be applied to the water-ethanol drop by the Teflon® block without the drop adhering to it. Under the applied pressure, the drop deformed far enough to come into contact with the small-scale features. The superhydrophobic nature of the small scale geometries prevented the liquid from fully wetting into the surface. In Figure 3.4(c), the physical pressure was reduced. However, the change in curvature was not great enough to overcome the force of adhesion between the drop and the small-scale structures. In Figure 3.4(d), the physical pressure was completely released. As the drop was only in contact with the small-scale features, the force of adhesion between the drop and the bottom surface was very small. As the water drop returned to its

original curvature, it was able to overcome this small force of adhesion and separate from the bottom surface.

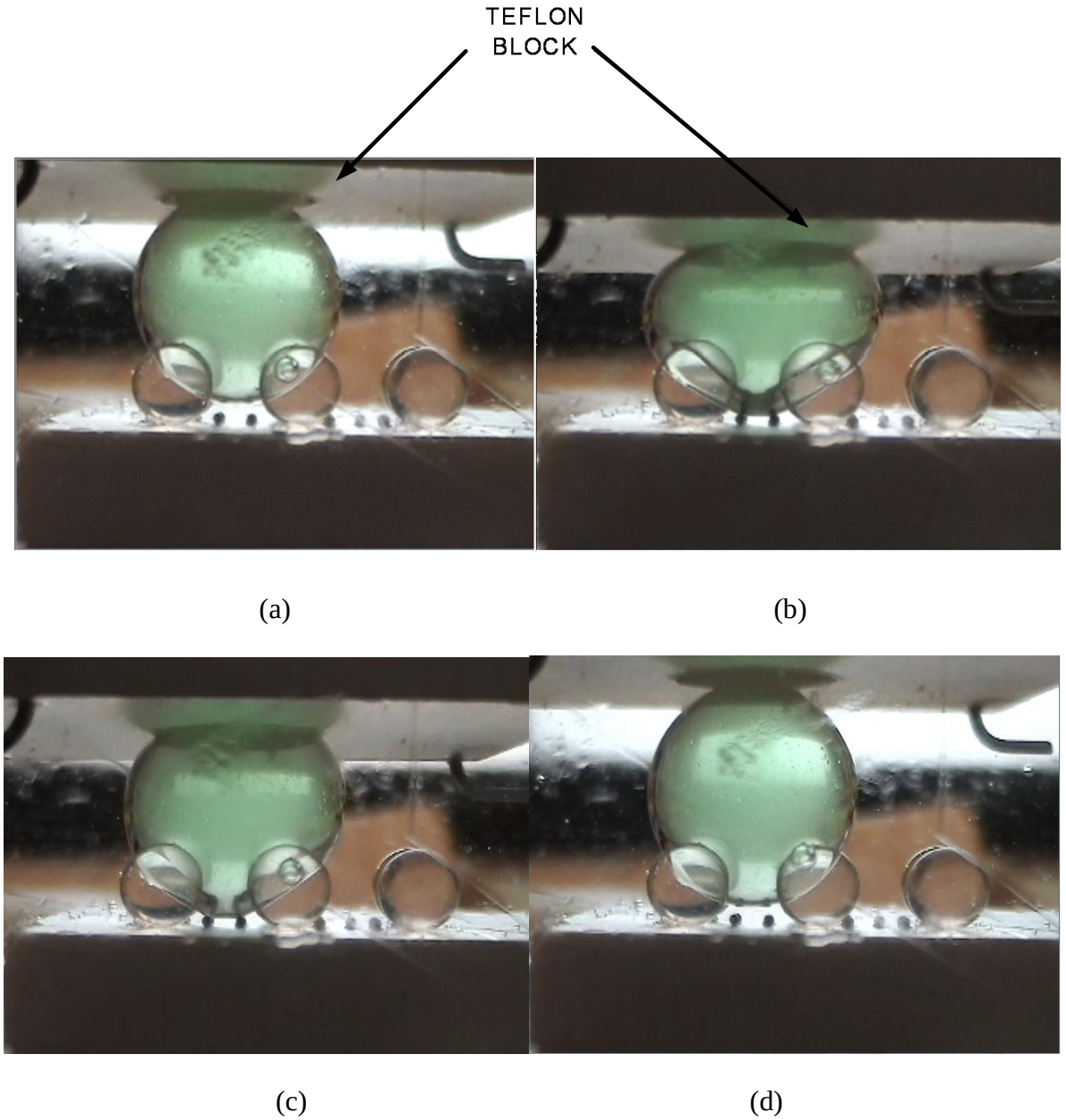

Figure 3.4: Neutral buoyancy simulation of a dual scaled surface a) Drop on dual scale structure with no applied pressure. b) Drop under applied physical pressure. c) Applied pressure being reduced d) Applied pressure fully released

3.5 Overhang Revisited

Now that the behavior of liquids on a sphere-covered surface has been demonstrated, it is useful to briefly return to the discussion of overhanging structures. The behavior of a liquid on an array of spheres provides a simple illustration of the behavior of liquids on an overhanging structure under applied pressure. Imagine a liquid supported by a surface covered with spheres as drawn in Figure 3.5. For simplicity, the liquid has an intrinsic contact angle of 90º with the spheres. Under zero applied pressure, the liquid interface has a curvature of zero and the liquid simply finds its contact angle at the equator of each sphere (Figure 3.5(a)). Under an applied pressure, the radius of curvature of the liquid interface decreases according to Equation (12). The contact lines of the liquid move down along the spheres such that the contact angle remains constant, and the curvature of the liquid matches the pressure applied (Figure 3.5(b)). Due to the overhanging nature of the spheres, the contact line is able to move under applied pressure without fully wetting into the surface. If the pressure is removed, the liquid simply returns to the original position. In this way, a surface covered with spheres is able to resist wetting under applied pressures.

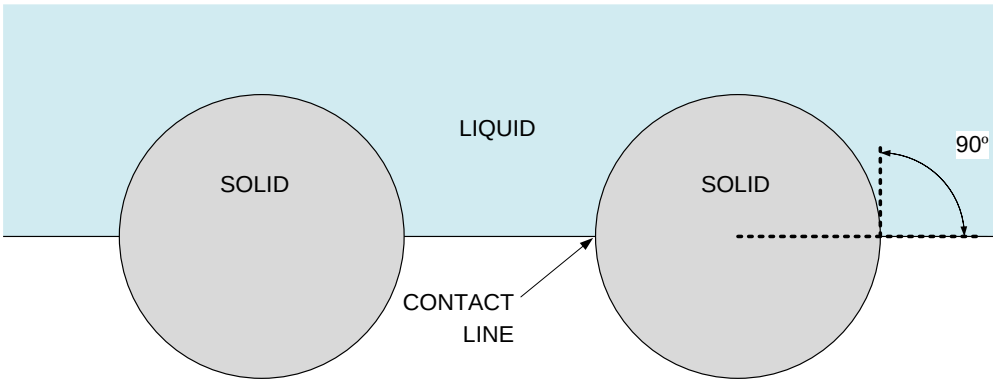

(a)

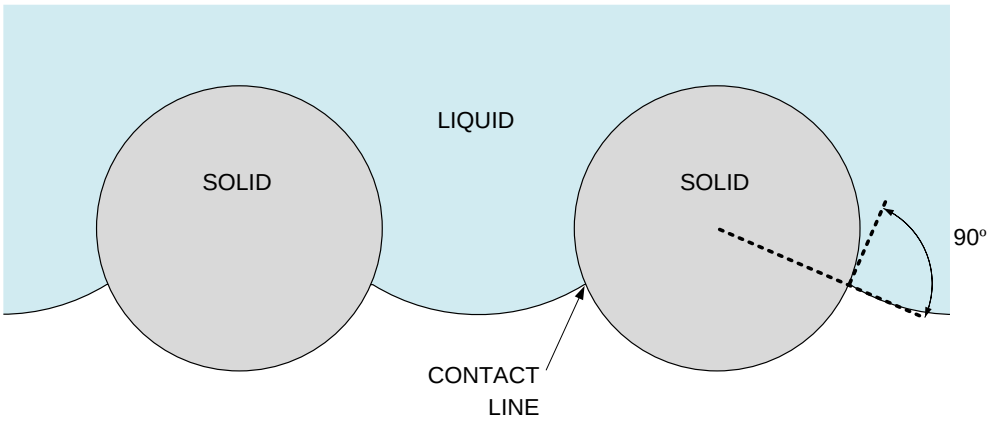

(b)

Figure 3.5: Liquid resting on spheres under a) no applied pressure and b) applied pressure

3.6 Alternative Simulations

The neutral buoyancy visualization technique clearly illustrates the importance of intrinsic contact angles in the design of superhydrophobic surfaces and can be used in the design and modeling of complex superhydrophobic structures. However, there are practical limitations to this method. For example, it is difficult to achieve arbitrary intrinsic contact angles between the liquid and solid surfaces, since appropriate surface materials and immiscible, neutrally buoyant liquids must be found for different contact angles.

An alternative to this approach is to use computer simulation with available software. One such program is Surface Evolver [30], a publicly available program that finds solutions of a surface by iteratively minimizing the energy of a surface under a given set of constraints. These constraints can include such things as pressure and contact angles. Surface Evolver has been used by a number of researchers in the study of the wetting behaviors of structured surfaces[31,32,33].

4 TRANSPARENT SUPERHYDROPHOBIC SURFACES

Superhydrophobic surfaces must be both chemically hydrophobic and physically porous, that is, a convoluted surface that traps air. If optical transparency is also desired, then the roughness of the surface must be limited to surface features that are smaller than the wavelength of visible light, the wavelength of visible light being between 390 and 750 nm. Surface features that are larger than a wavelength produces scattering and reduces transparency. In this section, different experimental techniques used to produce transparent superhydrophobic surfaces are presented.

4.1 Hydrophobic Coatings

Fabricating a superhydrophobic surface requires a material that can produce the desired surface geometries as well as a surface that is chemically hydrophobic, that is, a surface with a high intrinsic contact angle. A material that can be formed with the appropriate surface roughness may not necessarily be chemically hydrophobic and in those cases, a coating can be applied to alter the surface chemistry. The hydrophobic coatings used to fabricate superhydrophobic surfaces must meet two requirements; they must completely coat the surface and they must not destroy the surface profile of the surfaces they coat. Two such coatings are presented that have intrinsic contact angles greater than 100º.

4.1.1 Silanes

Silanes are molecular compounds formed from silicon and hydrogen. Many silanes are used to alter surface properties of inorganic substances, such as wettability, by reacting with and forming stable covalent bonds with the inorganic substance [34]. Silanes are especially suitable for surface modification of structured surfaces to produce superhydrophobic materials because of their ability to form a very thin and conformal monolayer. This results in a chemically uniform surface with little alteration to the surface geometry.

Octadecyltrimethoxysilane was chosen for these experiments since as a result of its long molecular chains, the molecule deposits in a densely packed layer. Silane deposition was

carried out by submerging a substrate in a solution of octadecyltrimethoxysilane in toluene, and the standard operating procedure is presented in Appendix A. The intrinsic contact angle between water and a smooth surface coated with octadecyltrimethoxysilane was measured to be 101±1°.

4.1.2 Teflon® AF

Teflon® AF compounds are amorphous fluoropolymers that are optically clear and soluble in certain solvents such as the Fluorinert™, FC-75[35] from 3M™. Teflon® AF dissolved in solution is suitable for spin coating thin films whereby the thickness of the film can be controlled by both spin speed as well as the concentration of Teflon® AF in solution. The intrinsic contact angle between water and Teflon® AF was measured to be 110±1°.

It was found experimentally that a single coating of Teflon® AF on a porous surface was not able to produce the desired results of superhydrophobicity, since a single coating that was thick enough to ensure complete coverage of the porous surface was found to in drastically alter the surface's geometry, causing loss of porosity. However, thinner coatings incompletely covered the surface, leaving parts of it exposed and producing a chemically inhomogeneous surface. The solution to this problem was to coat the sample multiple times with thin coatings. This ensured complete coverage of the surface while retaining its porosity.

4.2 Porous Surface Structures

Two methods of producing porous surfaces were explored to produce materials with surface geometries suitable for superhydrophobicity.

4.2.1 Glancing Angle Deposition Films

4.2.1.1 Deposition Technique

Glancing Angle Deposition (GLAD) is a thin film deposition process by physical vapor deposition (PVD) developed at the University of Alberta, Canada[36]. PVD is carried out in a vacuum chamber, where a source material is heated to the point of evaporation. This causes atoms or molecules of the source material to be ejected into the vacuum chamber. The atoms or molecules travel in a straight path, and the ones that are incident on a substrate will form nuclei and coalesce, creating a film of source material on the surface. In traditional PVD, the substrate surface is normal to the source material, as illustrated in Figure 4.1, and a continuous film is formed.

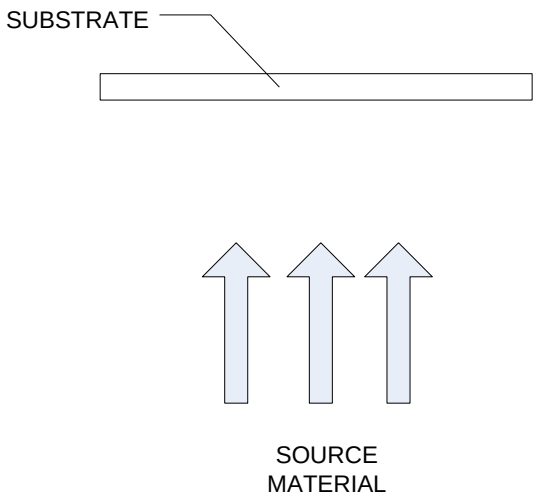

Figure 4.1: Traditional PVD deposition with substrate surface normal to the source material

If the substrate is tilted so that the surface is incident to the source material at an oblique angle, α, illustrated in Figure 4.2, then a porous film will form instead of a continuous one. This occurs due to shadowing during deposition, wherein atoms already deposited on the substrate will shield the area behind them. As this continues, a porous film of slanted

columns will form. The level of porosity is controlled by the amount the substrate is tilted, with a greater incident angle, α, resulting in a more porous film[37].

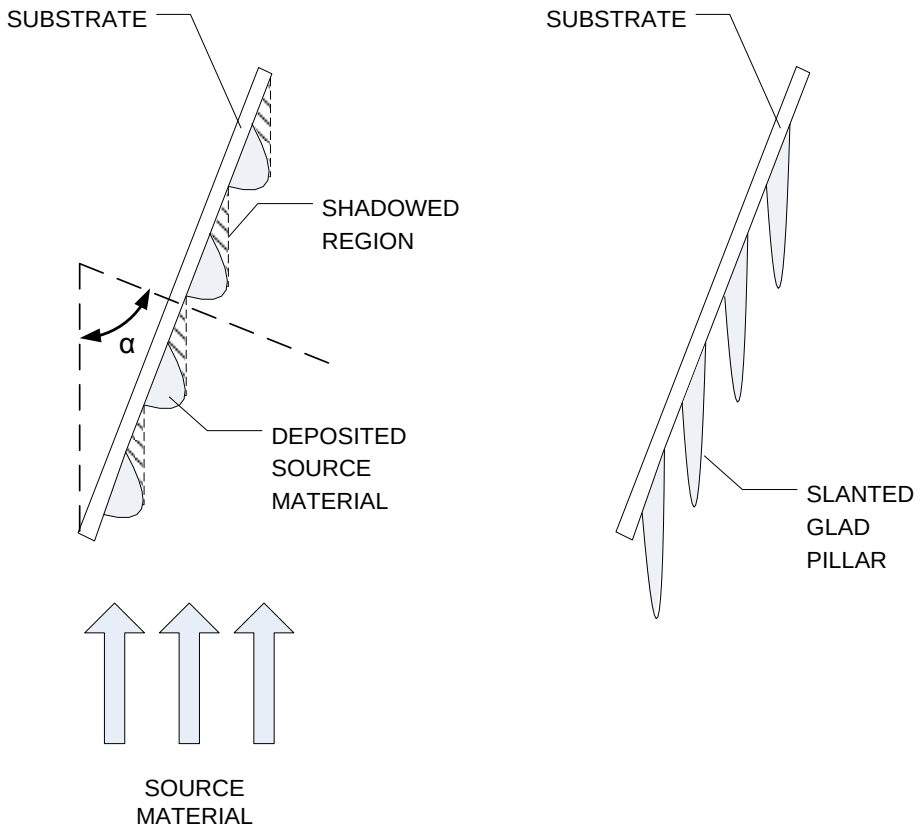

Figure 4.2: Slanted post GLAD films form on a tilted substrate

Further control of film geometry can be obtained by rotation of the substrate around an axis perpendicular to it, as illustrated in Figure 4.3. With this rotation, more complex surfaces such as chevrons and helices can be made[38]. If the rotation speed φ is constant and fast, then vertical post films are formed. Typical conditions for vertical post GLAD films are a rotation speed of 17 RPM and a deposition rate of 18 Angstroms/second. Other work has determined that for superhydrophobic surfaces, vertical post GLAD films are the most suitable of the GLAD geometries[39].

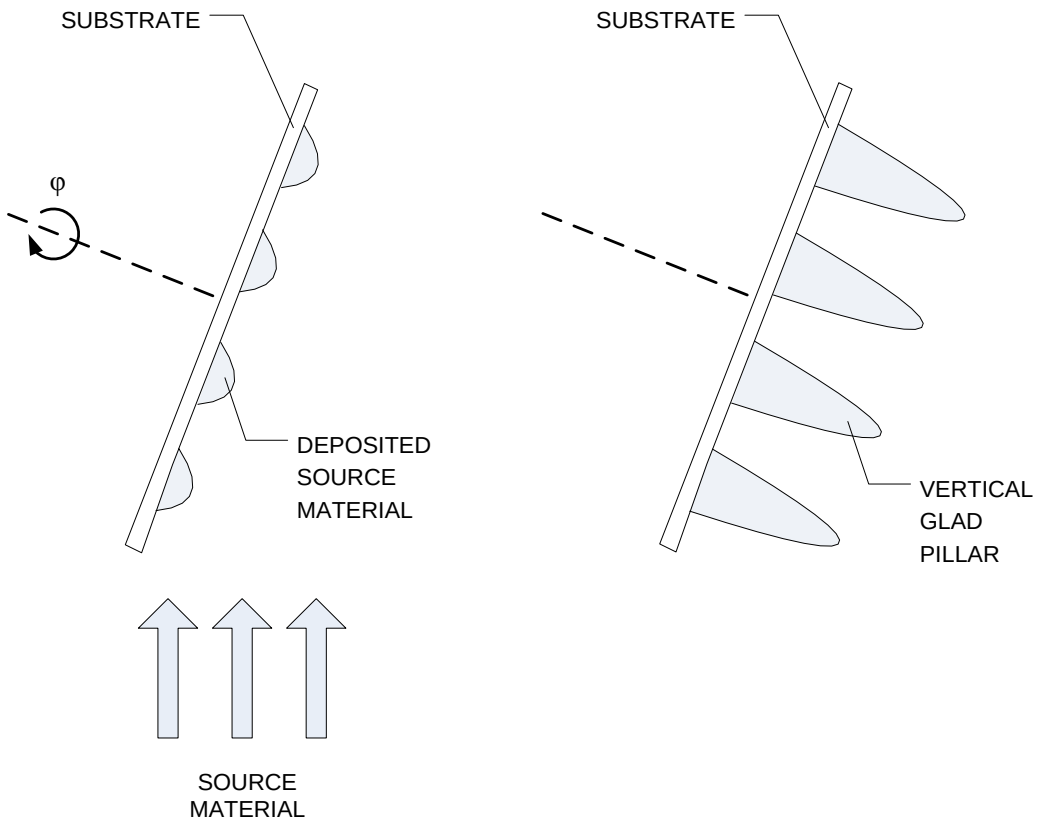

Figure 4.3: Vertical post GLAD films form if the substrate is rotated about an axis normal to it

4.2.1.2 ITO GLAD Films

GLAD films fabricated using indium tin oxide (ITO) were provided for this study by the Glancing Angle Deposition Research Group at the University of Alberta. ITO is a transparent conductor that can deposited as thin films. Vertical post ITO GLAD films deposited at an angle of 85º to the deposition source were used for their high porosity. The porous nature of the films is evident in the scanning electron microscope (SEM) image, Figure 4.4.

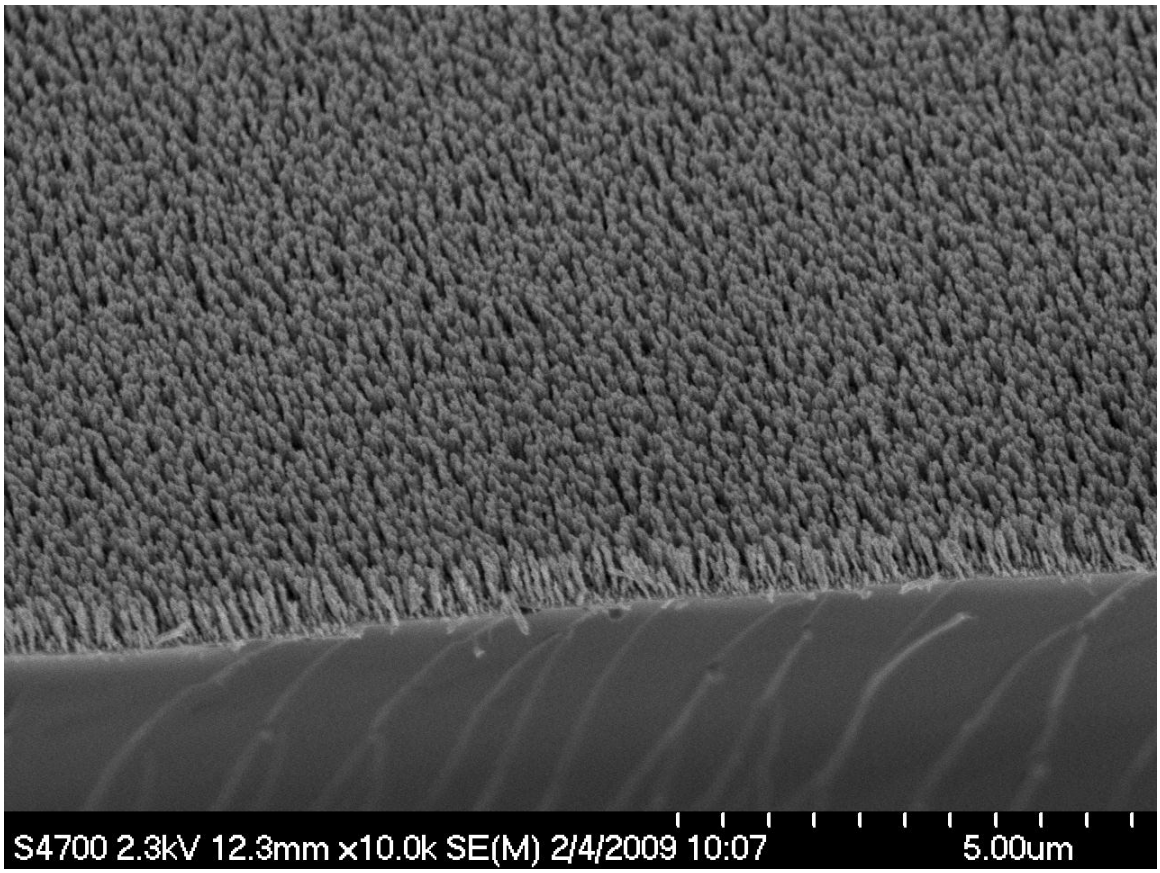

Figure 4.4: SEM image of ITO GLAD film at 10k magnification

At higher magnifications of 30,000x (Figure 4.5), the sharp, jagged geometry of the ITO pillars can be clearly seen. The ITO GLAD films were subjected to a coating of octadecyltrimethoxysilane via deposition in solution using the SOP outlined in Appendix A. The resulting film is superhydrophobic, with a contact angle of 153±1º and contact angle hysteresis of 7±2º.

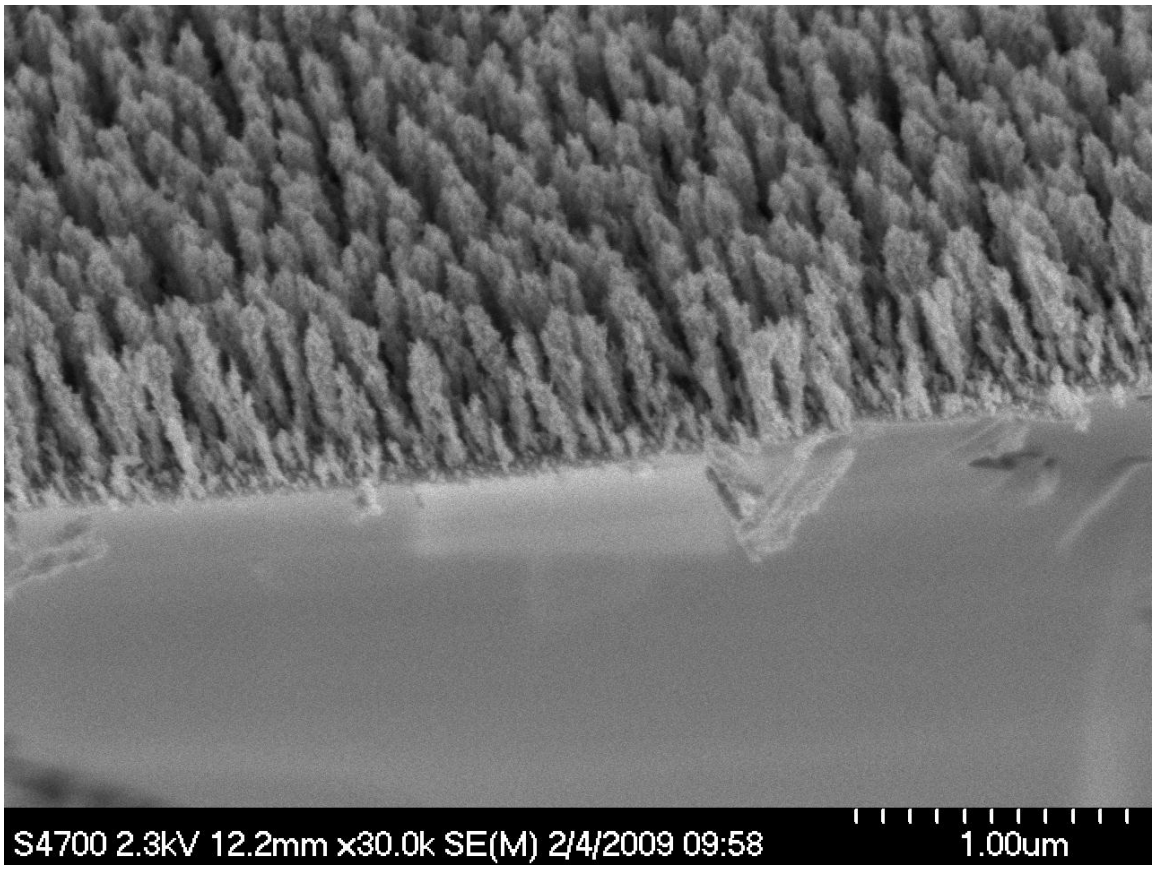

Figure 4.5: SEM of ITO GLAD film at 30k magnification

4.2.1.3 Silanized SiO_2 GLAD Films

ITO GLAD films are electrically conductive, and therefore unsuitable for experiments involving electrostatic deformation. Electrostatic deformation occurs due to charge build-up on the liquid surface when an electrical potential difference is applied between the liquid and an electrode. If the liquid makes electrical contact with the electrode, then the electrical potential difference between the liquid and surface becomes zero, and the charge build-up dissipates. For this reason, electrically insulating vertical post GLAD films made of SiO_2 were fabricated at the University of British Columbia. The SiO_2 GLAD films were fabricated in an electron beam evaporator outfitted for Glancing Angle Deposition. However, because only vertical post GLAD films were needed, the setup was simplified as changes to the substrate angle and rotation speed during deposition were not required. This eliminated issues such as constructing mechanical and electrical feedthroughs into the vacuum chamber.

The setup for Glancing Angle Deposition is described in Appendix B. SiO_2 GLAD films were made with the following parameters:

Table 4.1: Parameters for fabrication of SiO_2 GLAD films

Deposition Parameter	**Value**
Deposition angle	85º
Rotation Speed	16 RPM
Deposition Rate	10 A/s
Chamber pressure	1.5E-6 Torr

However, upon deposition of octadecyltrimethoxysilane, SiO_2 GLAD films did not become superhydrophobic, as confirmed by the resulting contact angle measurements of 100±1º. It was thought that this was a result of the difference in geometries between ITO and SiO_2 GLAD film pillars. As can be seen in Figure 4.6, the SiO_2 GLAD films consisted of pillars that were much smoother than the jagged pillars of their ITO counterparts, and this jaggedness provided multiple-scale roughness on the ITO GLAD films. Further experiments were conducted on SiO_2 GLAD films using coatings of Teflon® AF.

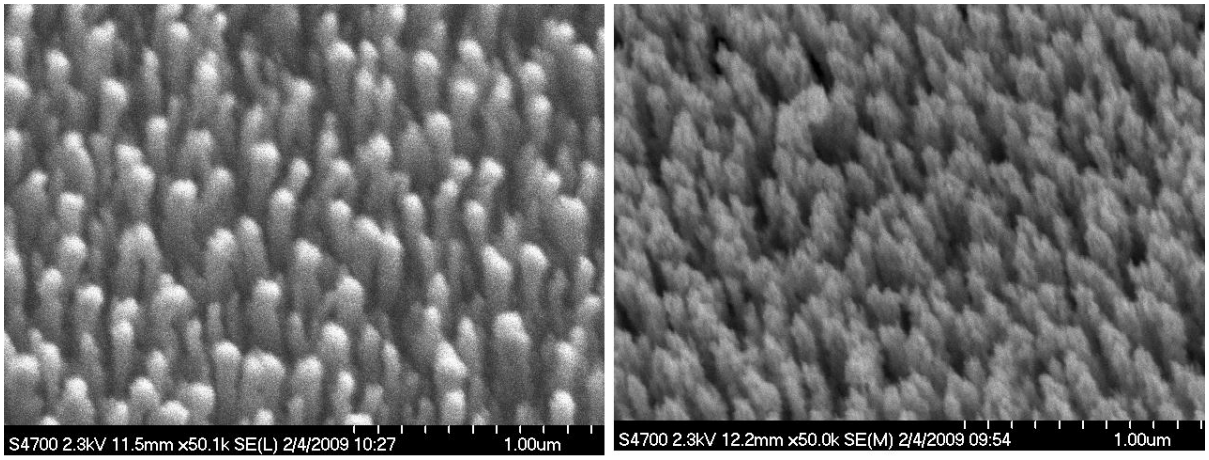

(a) (b)

Figure 4.6: Comparison of a) SiO_2 and b) ITO GLAD Films at 50k magnification

4.2.1.4 Teflon® AF Coated SiO2 GLAD Films

The SiO_2 GLAD films were also coated with Teflon® AF via spin coating. After coating, the surfaces exhibited a much higher contact angle than that of the silane-coated SiO_2 GLAD films. The Teflon® AF-coated films have a contact angle of 145±1º and contact angle hysteresis of 18±2º. The difference between octadecyltrimethoxysilane and Teflon® AF coatings was thought to occur from the enhancement of overhang features that Teflon® AF had on the GLAD film post geometry. Figure 4.7 contains a comparison of the two surfaces as seen by SEM. The uncoated vertical posts in Figure 4.7(a) exhibit a slight overhang structure at the top of the posts that becomes exaggerated once coated with Teflon® AF (Figure 4.7(b)). The Teflon® AF coating also introduces a nano-scale surface roughness to the pillars, producing a surface with dual-scale roughness features. These small-scale roughness features also contributes to superhydrophobicity by acting as small overhang structures.

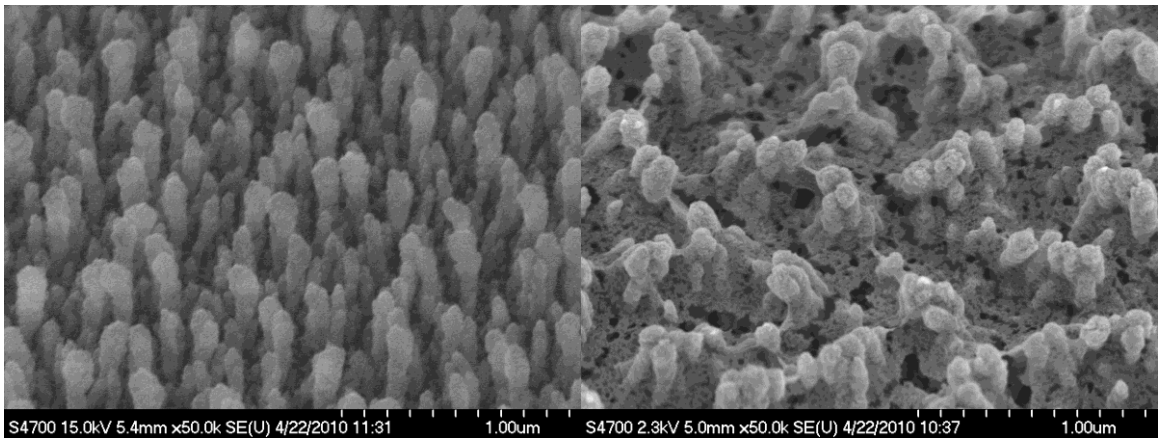

(b)

Figure 4.7: SEM Image of a) uncoated vertical post SiO2 GLAD film and b) Teflon® AF coated vertical post SiO_2 GLAD film at 50k magnification

A different technique for producing roughness features on the nanometer size scale was also explored and will be discussed in the next section. This technique was based on plasma etching, and was found to be a quicker, more versatile fabrication technique than GLAD in producing geometries suitable for transparent superhydrophobic surfaces.

4.2.2 Plasma Etched Polymethyl Methacrylate (PMMA) Films

4.2.2.1 Nano-scale Roughness by Oxygen Plasma Etch

Organic contaminant cleaning is often done in the field of microfabrication with a plasma clean. In this process, a gas is introduced to a low pressure vacuum chamber and subjected to an electromagnetic field, generating a plasma. An electrical potential accelerates the ions in the plasma towards a target substrate. In the specific case of oxygen plasma cleaning, organic material on the substrate is removed by a combination of chemical reactions and physical ablation[40]. These same processes can also be applied to etch features into an organic film.

When a film is plasma-etched, nano-scale contaminants on the surface of the film can act as nano-scale etch masks, causing non-uniform etching. This non-uniformity in etching produces nano-scale features in the resulting film[41]. By choosing suitable etch conditions,

this nano-roughness can be purposely enhanced, and superhydrophobic surfaces can be created[42].

Vourdas et al[43] fabricated optically transparent superhydrophobic surfaces on PMMA films by oxygen plasma etch in a helicon reactor followed by a Teflon-like deposition using C_4F_8 gas. Due to the nature of the helicon reactor, they postulated that aluminum particles were being deposited onto the sample during the plasma etching process, and this produced the nano-masking required to cause roughness on the surface.

We fabricated similar superhydrophobic films by roughening PMMA films on glass substrates using oxygen plasma etch in a reactive ion etcher and spin-coating with Teflon® AF dissolved in FC-75. The full SOP for fabricating superhydrophobic films this way can be found in Appendix C.

Figure 4.8 shows an SEM image of the roughness features produced on the surface of PMMA after oxygen plasma etch. The height difference between the peaks and valleys on the roughened surface is about 400 nm. Teflon® AF coating of etched PMMA films resulted in drastically altered surface geometries, as shown in Figure 4.9. This may have occurred if the rough surface features on the PMMA were only loosely held to the surface. The spin coat step during Teflon® AF coating may have swept away much of the surface structures, or the rough features may have been pulled together by surface tension as the Teflon® AF solvent evaporated.

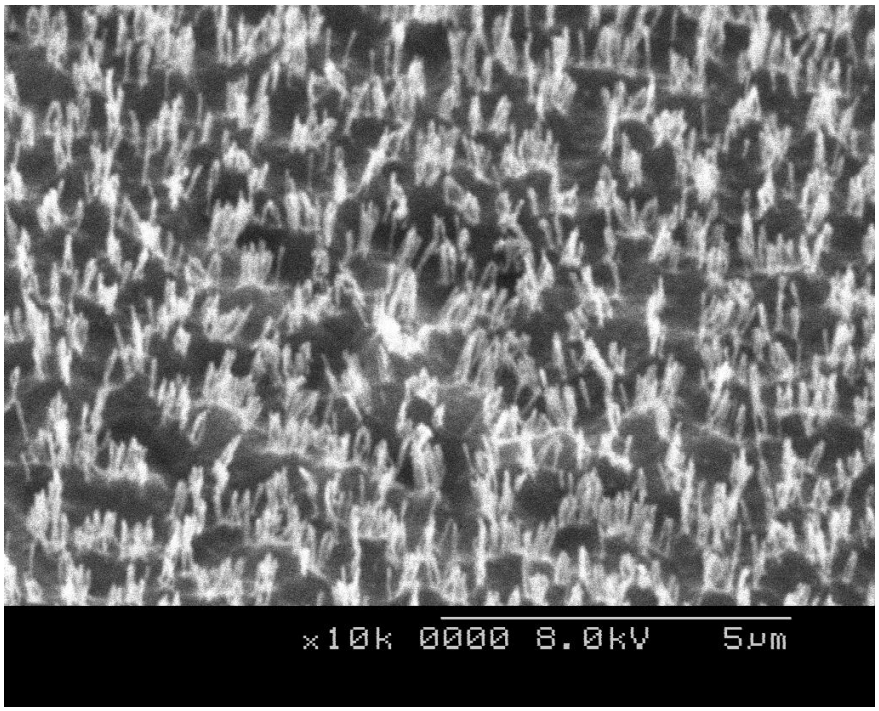

Figure 4.8: SEM Image of PMMA surface after oxygen plasma etch at 10k magnification

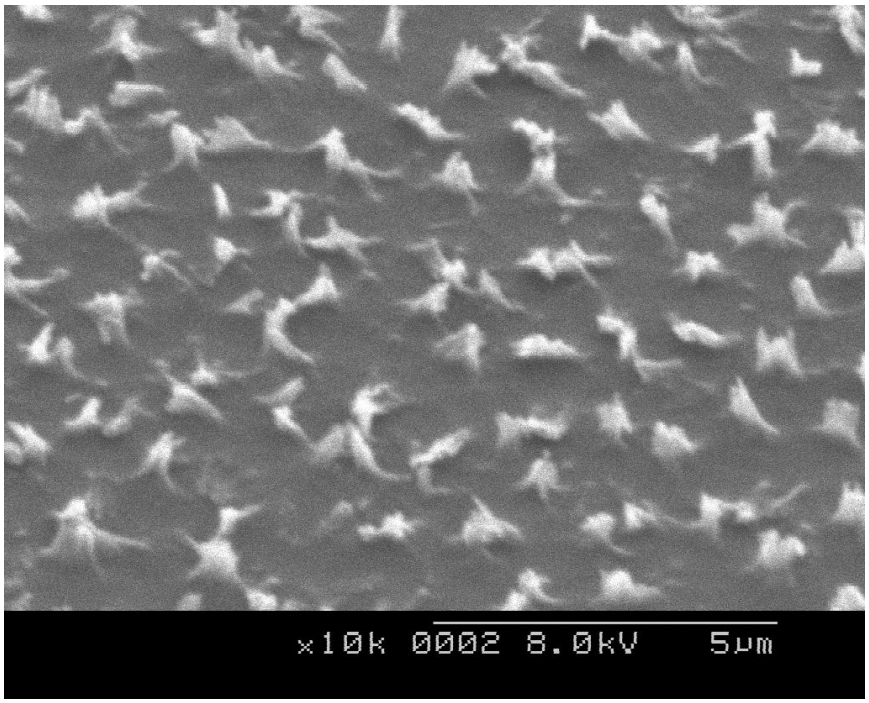

Figure 4.9: SEM image of plasma-etched PMMA film coated with Teflon AF at 10k magnification

Teflon® AF coated PMMA films resulted in contact angles of 159±1º and contact angle hysteresis of 6±2º. Silane coating in solution was not attempted as PMMA is not chemically resistant to the solvents used in that process.

4.2.2.2 Robustness of superhydrophobic PMMA films

The period of time that elapsed between oxygen plasma etching and Teflon® AF coating was found to critically affect the robustness of the resulting superhydrophobic films. PMMA films coated with Teflon® AF the same day that they were plasma etched showed noticeable differences from samples that had a one day delay between etching and Teflon® AF coating. This was thought to be due to the cleanliness of the PMMA surface. The pristine surface of the PMMA, free of contaminants, immediately after plasma etching provides an ideal surface for Teflon® AF to coat. Over time, contaminants accumulate on the PMMA surface, and this is detrimental to Teflon® AF coating.

For samples that were Teflon® AF coated more than one day after plasma etching, a low power oxygen plasma clean was found to promote adhesion of Teflon® AF. The power density of this plasma clean was 1590 W/m^2. In comparison, the plasma etch that produced the surface roughness features had a power density more than ten times greater, 16,700 W/m^2. This low power clean was kept short (10 seconds) to ensure that the etched roughness was left unaltered. Samples that were Teflon® AF coated immediately after a low power oxygen plasma clean were found to be as robust as freshly etched surfaces.

4.2.2.3 Optical properties of superhydrophobic PMMA Films

Optical transparency is an important property of the superhydrophobic films for the purposes of this study. However, we are most concerned with the reflectance properties when light strikes the surface at an angle of incidence past critical angle and undergoes total internal reflection. We are also interested in the change in reflectance of light when a high index material is placed within the evanescent region, and cause the light to undergo frustration of

TIR. The amount of light undergoing TIR that becomes frustrated by a nearby high index material is dependent on the incident angle of light, as the penetration depth of the evanescent wave is dependent on the incident angle. Thus, simple transmission and reflectance measurements of the films did not provide sufficient information and reflectance measurements where the angle of incidence of light was adjusted were required.

4.2.2.3.1 Experimental Setup for Measurement of Frustrated Total Internal Reflection

The behavior of incident light past critical angle at a superhydrophobic PMMA interface was studied using the setup illustrated in Figure 4.10, which is not drawn to scale. In it, an acrylic, right angle prism coupled light from a laser diode with wavelength of 650 nm and power of 5mW to and from the PMMA sample surface. Optical contact between the coupling prism and sample was made using type A immersion oil[44], which has an index of refraction of 1.515. This is quite close to the index of refraction of both the acrylic prism and the glass substrate of the sample. The intensity of the reflected light was measured by a photodetector, TSL 257[45] from Texas Instruments, inside of an integrating sphere cavity, which is a hollow cavity with an opening, the inside of which is lined with an optically diffuse, highly reflective material. Light striking any point inside of the integrating sphere cavity and from any direction will illuminate the entire inner surface of the cavity with the same power per unit area. Thus, an optical intensity measurement taken inside the integrating sphere measures relative optical power, while eliminating spatial effects such as the incident direction of light[46]. Frustration of total internal reflection was studied by placing a water drop on the sample surface. The water drop was supported by the 400 nanometer-high surface features of the transparent superhydrophobic film, and was thus within the evanescent wave region, allowing it to couple out a portion of light normally undergoing TIR. The laser was mounted on a tilt stage, the MXT Angle Platform[47], which allowed adjustment of the angle the laser made with a horizontal. This tilt stage provided angular adjustments as fine as 0.1°.

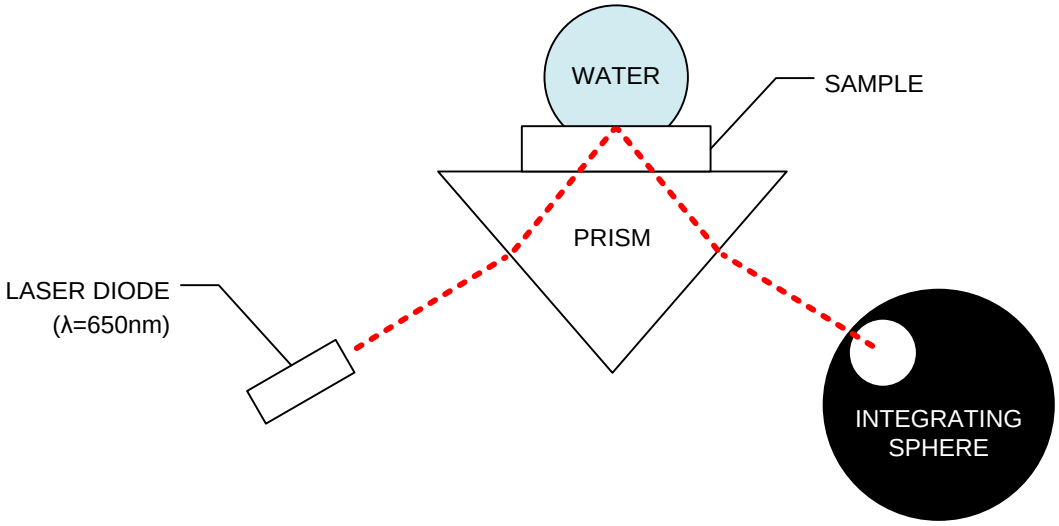

Figure 4.10: Experimental setup for study of reflectance of superhydrophobic PMMA films

4.2.2.3.2 Simulation with GSolver©

The optical properties of the transparent superhydrophobic films were also investigated with a theoretical model of the porous films using GSolver© [48]. GSolver©, a commercially-available software package, uses rigorous coupled-wave (RCW) analysis and is useful for finding solutions to the reflected and transmitted intensities of light incident on diffraction gratings and thin films. In RCW, Maxwell's equations are solved exactly with a truncation of the Fourier expansion of the permittivity of each layer[49].

When water rests on top of the transparent superhydrophobic PMMA film, the resulting optical system can be thought of as shown in Figure 4.11(a). The PMMA film consists of a solid PMMA substrate layer on top of which sit PMMA features with a height of 400 nm. Air is trapped between the PMMA roughness features. Water rests on top of this layer of PMMA and air. As the water is kept a distance of 400 nm from the solid PMMA surface by the PMMA protrusions, the water is within the evanescent region and a portion of light traveling through the PMMA and incident at its surface beyond critical angle will be frustrated by the water.

Because the PMMA film structures are sub-optical wavelength in size, we can simplify the GSolver© simulation by approximating the porous PMMA film as homogenous films with

effective indices of refraction. In our simulations, two thin films having refractive indices of 1.25 and 1 were used to approximate the porous PMMA layer, as illustrated in Figure 4.11(b).

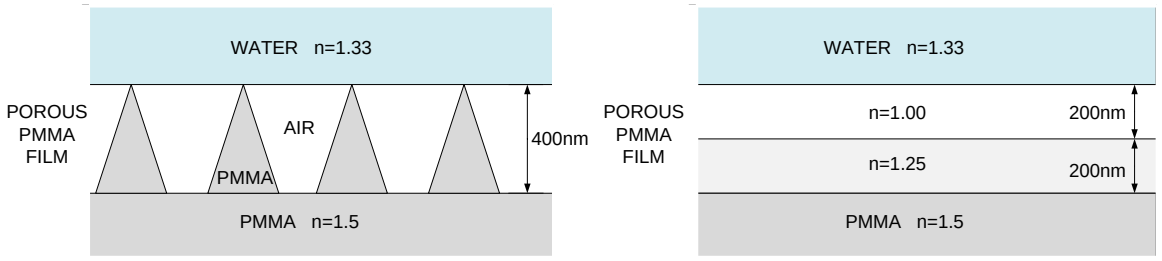

(a) (b)

Figure 4.11: a) Experimental PMMA film structure and b) representation in GSolver© software

4.2.2.3.3 Experimental and Simulation Results of Reflectance of Porous PMMA Films

A comparison of the experimental and simulated reflectance values as a function of incident angle is shown in Figure 4.12. The reflectance is shown for both the case of total internal reflection and frustrated total internal reflection by water entering into the evanescent region and making optical contact with the PMMA surface. For the total internal reflection case, the water was removed and replaced with air.

Experimentally, the reflected intensity of light incident at an angle 1.5º greater than critical angle is reduced by 45% when light is frustrated by water at the superhydrophobic surface. As such, these samples are suitable for experiments involving reversible frustration of TIR, as discussed in Chapter 5. That is to say, the difference between the reflected intensity of light undergoing TIR and undergoing frustration of TIR by water is significantly large to allow for the study of reversible modulation of reflectivity.

The average root mean square difference between each of the experimental reflectance measurements and those simulated by GSolver© was 10.1%. A better fit to the data could be obtained by modeling the porous layer with a greater number of thin films or by modeling the

actual geometries of the porous film. For our purposes, GSolver© was used as a simple check to determine the thickness of porous PMMA films that allowed for substantial frustration of TIR and greater accuracy was unnecessary.

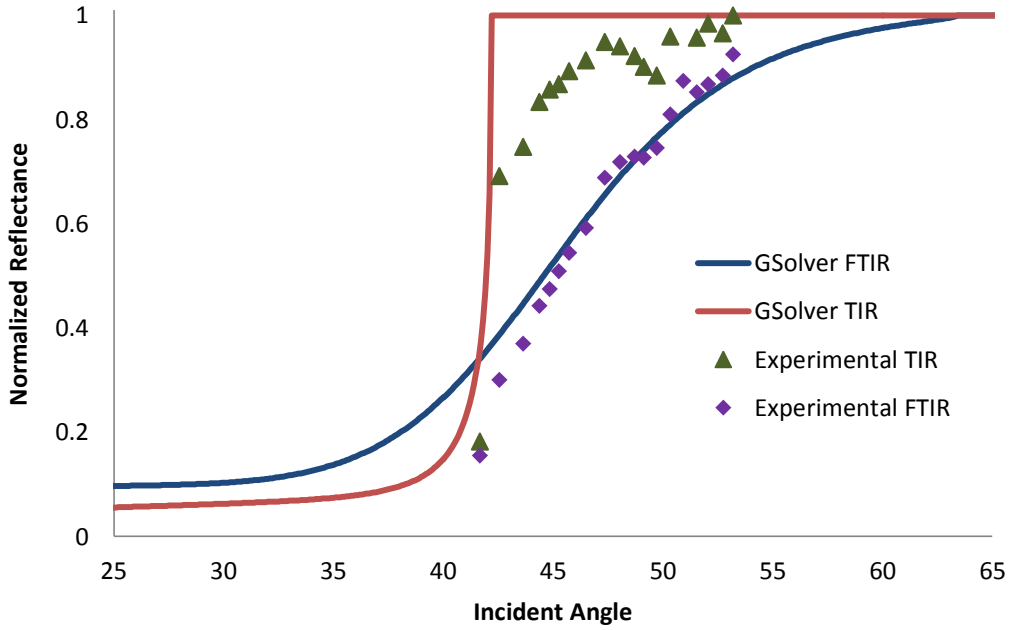

Figure 4.12: Experimental reflectance and simulated reflectance by GSolver© as a function of angle of incidence of a porous PMMA film

4.3 Force of Adhesion of Superhydrophobic Surfaces

An important property of superhydrophobic surfaces is the force of adhesion between the surface and water. This is the force required to completely separate a drop of water from a surface. A numerical calculation, the details of which are outlined in Appendix D, was done to find the adhesion force of a surface given its contact angle and volume. The results of this calculation were experimentally verified by using a mass measurement scale with an accuracy of 1 mg. The force required to separate a water drop from a silanated ITO GLAD film was experimentally measured by this scale to be 1.96E-5±0.98E-5 N. The calculated force of adhesion using the method outlined in Appendix D is 1.78E-5 N.

4.4 Conclusions

Teflon® AF coated PMMA films were chosen as the best candidate for experiments related to reversible frustration of TIR. This was due to its relative ease of fabrication, easily changed etch parameters, and acceptable superhydrophobic and optical properties. Plasma etch of PMMA is much faster to do than GLAD film deposition. Plasma etch of a single PMMA sample takes about 10 minutes. In comparison a single SiO_2 GLAD film takes several hours to make, mainly due to the time it takes for the PVD chamber to pump down to an acceptably low pressure. The size and spacing of the roughness features on plasma-etched PMMA films are also easily changed by adjusting a variety of parameters of the plasma etch. Chamber pressure, power, etch time, and gas flow rate are all easily adjustable parameters that affect the resulting PMMA film geometry. This allows the plasma etch to be adjusted such that the resulting PMMA films have an acceptable level of both superhydrophobicity and transparency. Due to these factors, plasma etched PMMA films with Teflon® AF coatings were used in the devices described in the next chapter.

5 ELECTRICAL CONTROL OF TIR ON SUPERHYDROPHOBIC STRUCTURES

In this section, we describe the design, operation and experimental demonstration of devices capable of electrically controlled, reversible frustration of total internal reflection at a transparent superhydrophobic interface. For the sake of brevity, these devices will be referred to as FTIR devices.

5.1 Description of FTIR Devices

5.1.1 FTIR Device Design

The FTIR device consisted of two scales of superhydrophobic structures, as illustrated in Figure 5.1. The device consisted of a glass substrate coated with a layer of ITO. On top of the ITO was a transparent dielectric layer of PMMA, which was roughened by oxygen plasma etch and made superhydrophobic by Teflon® AF coating. The features of the PMMA film were approximately 400 nm high. Thus, when a material of higher refractive index, such as water, rested on top of these structures, the water would be within the evanescent wave region. Consequently, energy in the evanescent wave that had penetrated a distance beyond 400 nm would be coupled into the water and frustration of total internal reflection occurs.

The large-scale superhydrophobic structures of the device were two 150 μm high, vertical-walled structures running parallel to each other and spaced 600 μm wide, creating a trench-like geometry. The dimensions of these trench-like structures were chosen simply for ease of fabrication and were made of Scotch® Magic™ brand tape[50] due to its well defined, consistent thickness and availability. The Scotch® tape structures, hereby referred to simply as “trench structures”, were coated with a commercially available superhydrophobic coating, WX2100[51] from Cytonix. The WX2100 coating produces roughness on the sides of the trench structures, creating small overhang features on the sides of the trenches.

A water drop rested on top of the trench structures. The gap between the water and the superhydrophobic PMMA surface was approximately 100 μm. This distance is much greater than that of the evanescent wave region, and allows light incident at the PMMA surface

beyond critical angle to undergo TIR. A gold wire was inserted inside the water drop. This acted as the top electrode of the device. The ITO film beneath the superhydrophobic PMMA layer acted as the bottom electrode of the device. The ITO layer was prevented from coming into electrical contact with the water by the PMMA dielectric film, which was approximately 100 μm thick. Water is moved to and from the transparent superhydrophobic surface by application of electrostatic pressure, which is caused by a charge buildup at the water and ITO surfaces. If the water and ITO were to make electrical contact, than this charge buildup would dissipate, and the electrostatic pressure would be reduced to zero.

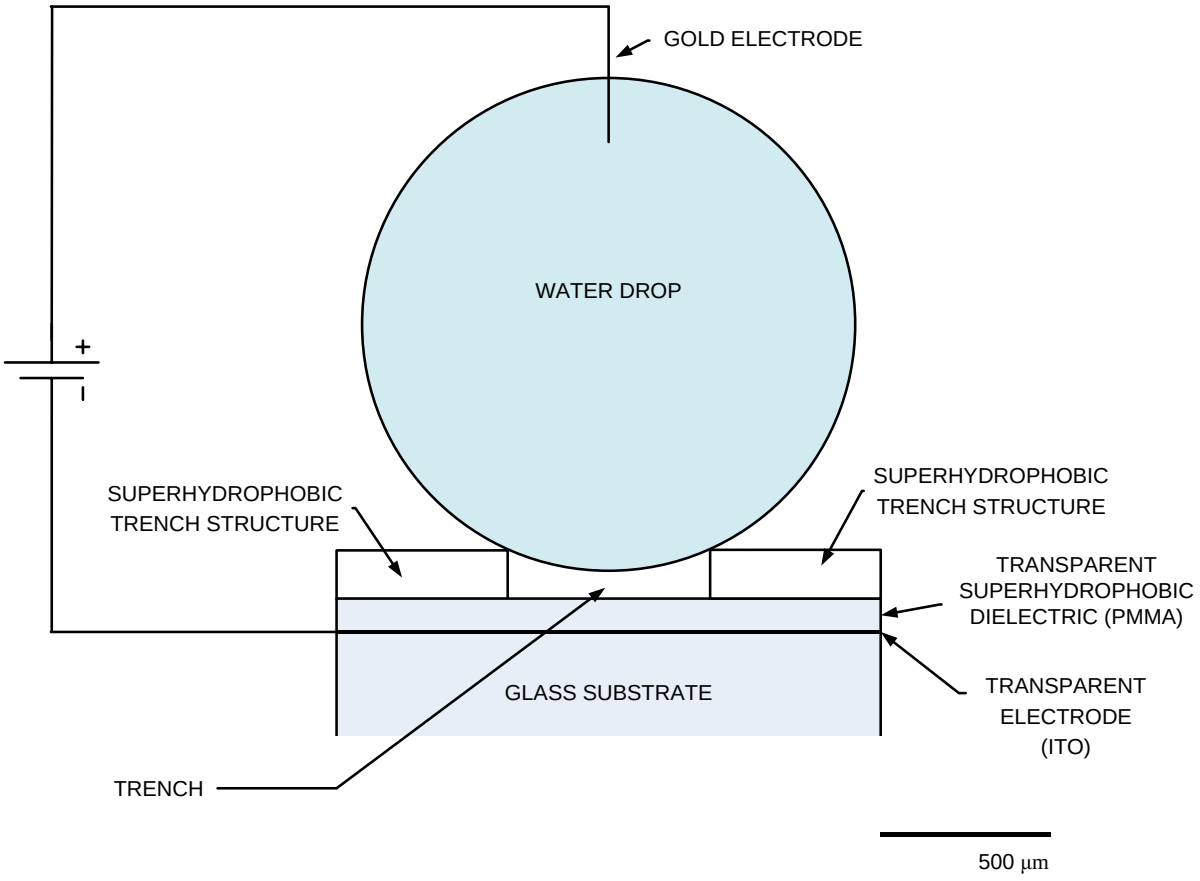

Figure 5.1: Structure of FTIR Devices

5.1.2 Operation of FTIR Devices

When the potential difference between the water and ITO electrode are zero, then the water drop rests on top of the trench structures well outside of the evanescent wave region and incident light past the critical angle is totally internally reflected, as shown in Figure 5.2(a), which is not drawn to scale. When an electrical potential difference is applied between the two electrodes, an electrostatic pressure is applied to the water, causing it to enter into the trench by decreasing its radius of curvature. If the curvature becomes great enough, the water will enter the evanescent region of light and a portion of the TIR light will be coupled into the water as shown in Figure 5.2(b). The water can only travel as far into the evanescent region as the tops of the PMMA roughness features. The superhydrophobic nature of the porous PMMA surface prevents the water from wetting into it. Thus, the size of the roughness features of the PMMA surface determines the maximum intensity of light that can be reversibly frustrated by this method, as the amount of light that is coupled out by frustration of TIR depends on the distance between the water and the solid PMMA surface.

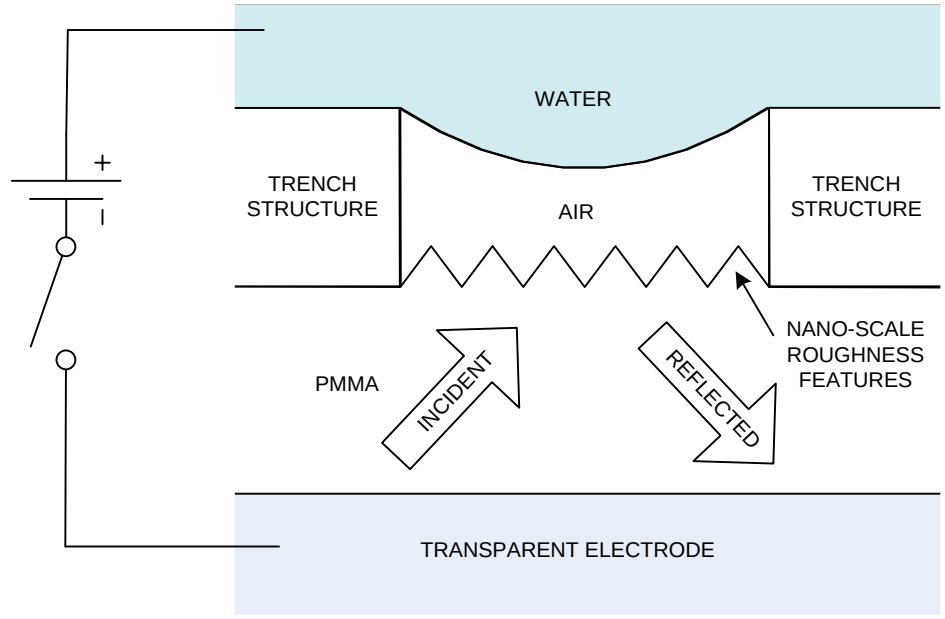

(a)

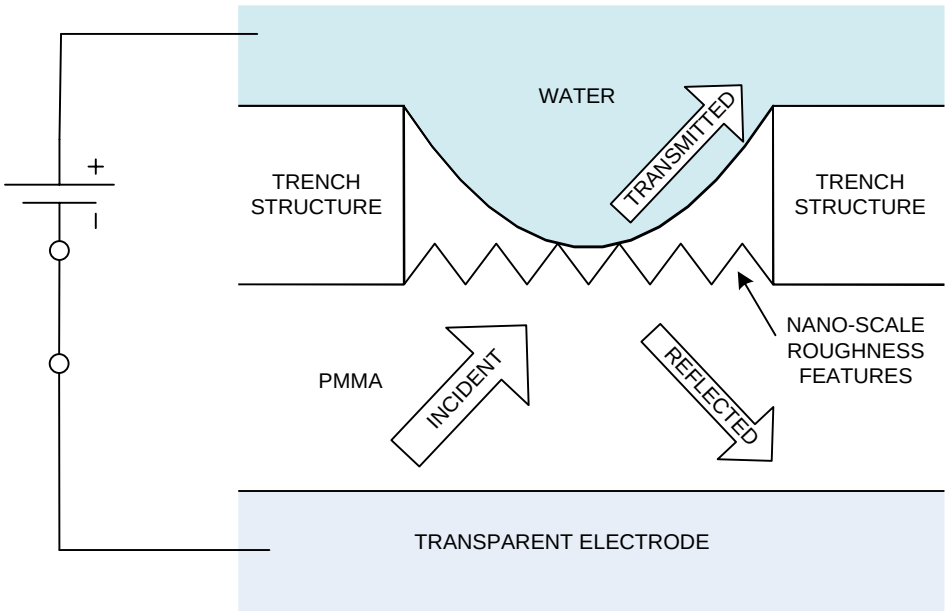

(b)

Figure 5.2: a) FTIR device under zero potential and b) device once potential is applied

When the potential is removed, the electrostatic pressure applied becomes zero and the pressure difference between the water drop and surrounding air returns to its original value. The water drop thus has a tendency to return to its original curvature due to this change in pressure. If the change in pressure is large enough to overcome the force of adhesion between the water drop and the superhydrophobic PMMA surface, than the water is able to separate from the PMMA surface. When this occurs, the incident light once again undergoes total internal reflection and the reflected intensity returns to its original value. In this way, reflectance can be reversibly modulated by application of the electrical potential.

5.1.3 Device Design: Trench Dimensions

The dimensions of the superhydrophobic trenches were chosen such that the difference in pressure of the water drop when no electrostatic pressure is applied and when the drop is in optical contact with the transparent superhydrophobic surface is large enough to overcome the adhesion force of the PMMA surface. However, this change in pressure, and therefore curvature, of the water drop cannot be made arbitrarily large. A larger change in curvature requires a greater electrostatic pressure to be applied to the water drop. If this pressure is too great, the water will wet into the porous PMMA surface, destroying the superhydrophobic nature of the surface, and causing the transition into the frustrated TIR state to be irreversible. Thus, it is desirable to find the minimum change in curvature that is still able to overcome the force of adhesion between the water and superhydrophobic PMMA.

The calculation to find the correct dimensions for the trench given a change in curvature of water is purely geometric, and the relevant dimensions are illustrated in Figure 5.3. For a given gap distance, *d*, between the bottom of the drop and the bottom of the trench, the radius of curvature of the water drop is calculated from the right angle triangle shown. The relationship is given in Equation (15).

$$R^2 = [R - (h - d)]^2 + \left[{}^{w}/_{2}\right]^2 \tag{15}$$

Rearranging we get an expression for *R* in Equation (16).

$$R = \frac{(h-d)^2 + ({}^{w}/_{2})^2}{2(h-d)} \tag{16}$$

With this relationship, it becomes a simple matter of choosing dimensions for the trench suitable for our purposes.

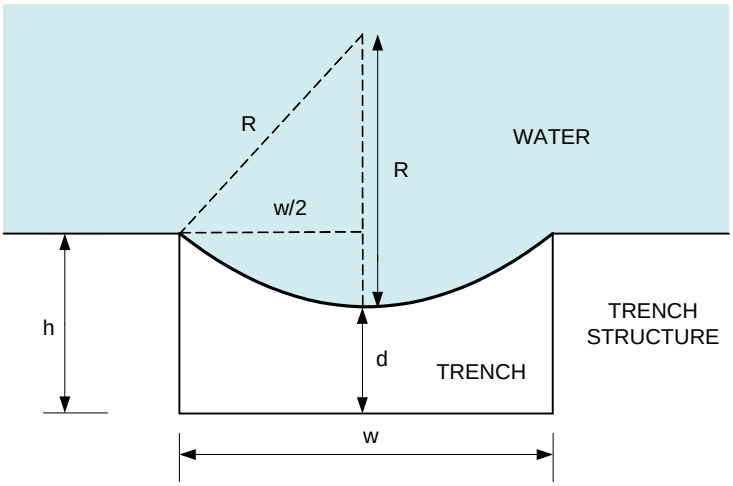

Figure 5.3: Dimensions of trench and water drop curvature

5.2 Experimental Setup

The experimental setup used to measure the reflectance of a FTIR device is shown, not to scale, in Figure 5.4. The device was put into optical contact with an acrylic, right angle prism using type A immersion oil with a refractive index of 1.515, which was similar to both the refractive index of the prism and the glass substrate of the device. Coupling the device to the prism allowed light past the critical angle to reach the PMMA surface, reflect by TIR, and exit the prism. A laser of wavelength 650 nm and power of 5 mW was mounted such that its emitted light was incident on the PMMA surface at an angle that was 1.5º beyond critical angle. This ensured that total internal reflection occurred. A photodetector, TSL 257 from Texas Instruments, inside of an integrating sphere cavity measured the intensity of the reflected laser light. An electrical potential applied to the FTIR device was produced by a transformer driven by a function generator. The function generator was required to produce an amplitude modulated sine wave, the reasoning of which is explained next. The

transformer was required as the function generator was not able to supply a large enough voltage by itself.

The function generator produced a 1 kHz sine wave which was amplitude modulated by a second function generator. The resulting output voltage was stepped up by a factor of 27:1 by a transformer and applied across the FTIR device. The frequency of 1 kHz was chosen to avoid complications due to the unpredictable movement of the water drop resulting from mechanical resonance of the drop. For the size of the water drops used, the resonant frequency was found to be around 100Hz. DC voltages were not used, as it was discovered that over time, the electrostatic pressure applied to the water drop under a DC potential would decrease. This was thought to be due to the finite conductance of air and PMMA. The air and PMMA layers in the FTIR device can be thought of as two capacitors in series, both with a parallel leakage resistance. Over time, under an applied DC electrical potential, the ratio of the voltages across the two layers simply becomes the ratio of the resistances across air and PMMA. Since air has a lower resistance than PMMA, the voltage, and therefore the electric field, across the air gap decreases over time. When the DC voltage is first applied, the voltage ratio between the air and PMMA layers is dependent on the capacitive components of each layer, rather than the resistive components.

The movement of the water drop on the superhydrophobic trench structure may also be affected by the different behaviors of contact line movement under AC and DC electric fields. For example, in one study of electrowetting, it was noted that contact angle hysteresis is smaller in the AC case as compared to the DC case[52]. Electrowetting involves changing the wetting properties of a liquid drop on a solid surface by applying an electrical potential between the liquid and an electrode underneath the solid surface.

A capacitor was inserted in series with the FTIR device, and its purpose is described in the next section.

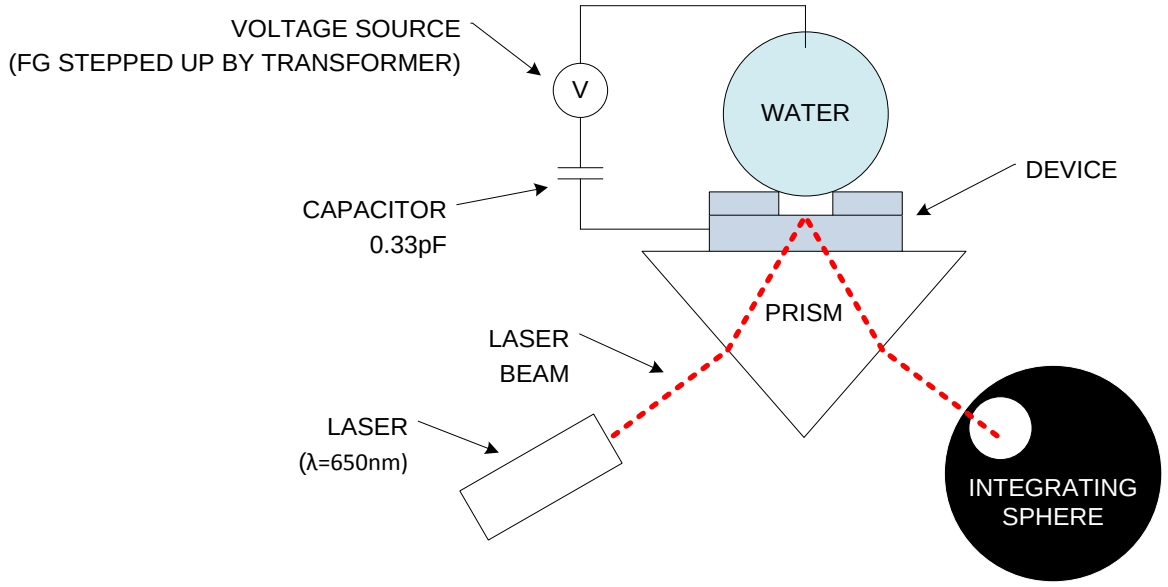

Figure 5.4: Experimental setup for characterization of optical response of FTIR device

5.3 The Runaway Effect

It was found experimentally that the electrostatic pressure required to bring the water into optical contact with the PMMA surface resulted in a pressure applied to the water that damaged the PMMA surface, causing the water to wet into the surface's pores. This problem is due to unnecessarily large electrostatic pressures applied to the water. Therefore, it was important to carefully calculate the optical electrostatic pressure that should be applied.

5.3.1 Calculation of Peak Voltage and Threshold Gap Distance

When the electrical potential difference applied across the FTIR device is increased, the gap distance between the water and PMMA surface decreases due to the decreasing radius of curvature of the water drop. As described in Section 5.1.2, the water drop has a tendency to return to its original curvature, and this tendency, which hereby will be referred to as the

restoring pressure, balances out the applied electrostatic pressure. It was found that as the electrical potential increases, there is a threshold voltage beyond which the restoring pressure of the water drop is no longer able to balance out the electrostatic pressure. At the corresponding gap distance between the water and PMMA at which this threshold voltage occurs, the voltage required to produce the electrostatic pressure necessary to hold the water at that distance decreases with decreasing distance. Figure 5.5 illustrates this problem, and is a plot of the calculated potential necessary to hold the water drop at different air gap distances. The air gap is the distance between the bottom of the water and the bottom of the trench. This air gap distance decreases with increasing electrical potential, as the potential causes the water to undergo electrostatic deformation. In Figure 5.5, for each gap distance, the applied voltage calculated produces an electrostatic pressure equal to the change in Young-Laplace pressure for the given deformation to occur (17).

$$P = \frac{\varepsilon_r \varepsilon_0 V^2}{2d^2} = \frac{\gamma}{r_{initial}} - \frac{\gamma}{r_{final}} \quad (17)$$

where $r_{initial}$ is the radius of curvature with zero applied potential and r_{final} is the radius of curvature at the given gap distance. The applied voltage does not reduce to zero as gap distance reduces to zero due to the finite thickness of PMMA dielectric coating on the ITO electrode.

The required electrical potential reaches a peak at the threshold gap distance. If the voltage is not quickly decreased for gap distances less than this threshold distance, then the system will experience a so-called runaway effect. This will cause the water to accelerate uncontrollably towards the PMMA surface, resulting in surface damage.

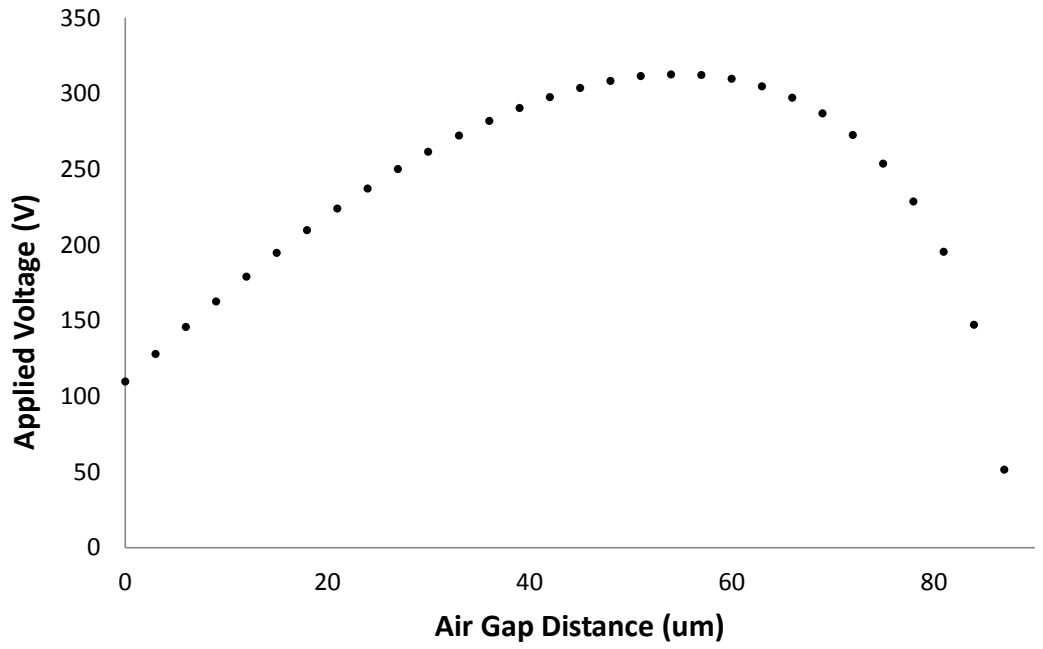

Figure 5.5: Applied voltage required to deform water to a given air gap distance. Dimensions of trench are 150 µm high and 600 µm wide

In addition, once the water makes contact with the superhydrophobic PMMA surface, the electrostatic pressure required to hold the water in that position is further reduced. This is due to the introduction of the adhesion force between the water and PMMA surface.

Thus, it is clear that the voltage required to maintain the water in optical contact with the PMMA surface is less than that of the peak voltage required to deform the water towards the surface. In fact, this high peak voltage is detrimental to the performance of the device.

5.3.2 Analogous MEMS System

The runaway effect described in the previous section is also encountered in the field of Microelectromechanical Systems (MEMS) actuators, and is best explained with an example of a simple MEMS system. Figure 5.6 illustrates a MEMS device consisting of two parallel electrodes and a spring. When there is no electrical potential applied between the two electrodes, the spring is in its equilibrium position and exerts no force. When a potential is

applied between the two parallel plates, the distance between them decreases until the restoring force of the spring balances out the electrostatic force. It is simple to show that when the distance between the parallel plates is two-thirds that of the equilibrium position, the spring is no longer able to balance out the electrostatic force at higher applied potentials. This results in a runaway effect and the parallel plates snap together.

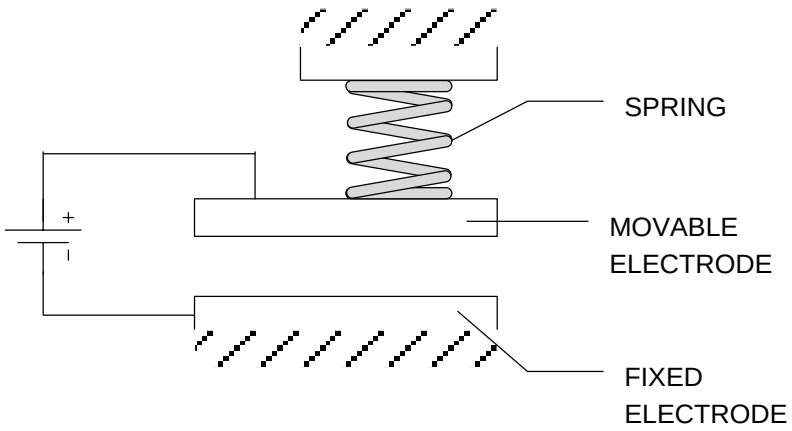

Figure 5.6: Analogous MEMS actuator system

An elegant solution to this was proposed by Seeger and Crary[53], whereby a capacitor is placed in series with the device. The MEMS device is essentially a variable capacitor; the capacitance of the MEMS device is dependent on the gap distance between the electrodes. By placing a capacitor in series with the MEMS device, the potential applied is divided between the two components. As the applied potential increases, the electrodes of the MEMS device come closer together, increasing its capacitance. This results in a greater proportion of the voltage being transferred to the series capacitor. If the value of the capacitor is properly chosen, then the runaway effect can be entirely eliminated. The tradeoff is that a higher potential must be applied to the whole system[54].

This MEMS actuator system is similar to the FTIR devices. The resistance of the water drop to deformation acts as the spring in our device, and the water drop and electrode form a variable capacitor dependent on the gap distance between them. A 0.33 pF capacitor was placed in series with the FTIR device to reduce the voltage applied once the water drop

reaches the PMMA surface. When water makes contact with the PMMA surface, the addition of the series capacitor theoretically reduces the voltage across the FTIR device by 5.2% and the electrostatic pressure by 10.1% in comparison to the FTIR device with no series capacitor. This improvement was found to be adequate to prevent the PMMA surface from becoming damaged under operation.

5.4 Experimental Data: Reflectance vs. Applied Voltage

The FTIR device described in Section 5.1 was experimentally demonstrated. Figure 5.7 plots the optical response of a device to multiple cycles of an applied potential signal, with a data sampling rate of 200 Hz. The applied electrical potential was in the form of a 1 kHz sine wave amplitude modulated by a 2 Hz square wave. The blue plot in Figure 5.7 is the normalized reflected intensity of the laser and the red plot is the amplitude of the applied potential across both the FTIR device and series capacitor. The normalized reflectance is calculated by:

$$Normalized\ reflectance = \frac{Reflected\ Intensity\ Measured}{Maximum\ Reflected\ Intensity\ Measured} \quad (18)$$

Upon application of an electrical potential with an amplitude of 280V, a 4% reduction of the reflectance from the maximum measured reflectance is seen and this optical response is repeatable over 15 modulating cycles. From the optical properties of the superhydrophobic PMMA films presented in Section 4.2.2.3, the expected change in reflectance is about 45%. This discrepancy can be accounted for by the difference between the laser spot size incident on the sample surface and the area of optical contact between the water and PMMA surface. This is reasonable as the size of the laser spot was approximately 8E-7 m^2 and the estimated area of optical contact between the water and PMMA surface was 7E-8 m^2. Thus, the area fraction of the laser spot size occupied by the area of optical contact was about 9%. The spot size of the laser was not reduced further as a reduction of the aperture size caused unwanted diffraction effects, and focusing the beam with a lens would have increased the angular spread. A possible solution to this in future experiments could be to mask the surface of the sensor such that only the portion of the laser spot that is of interest reaches the sensor.

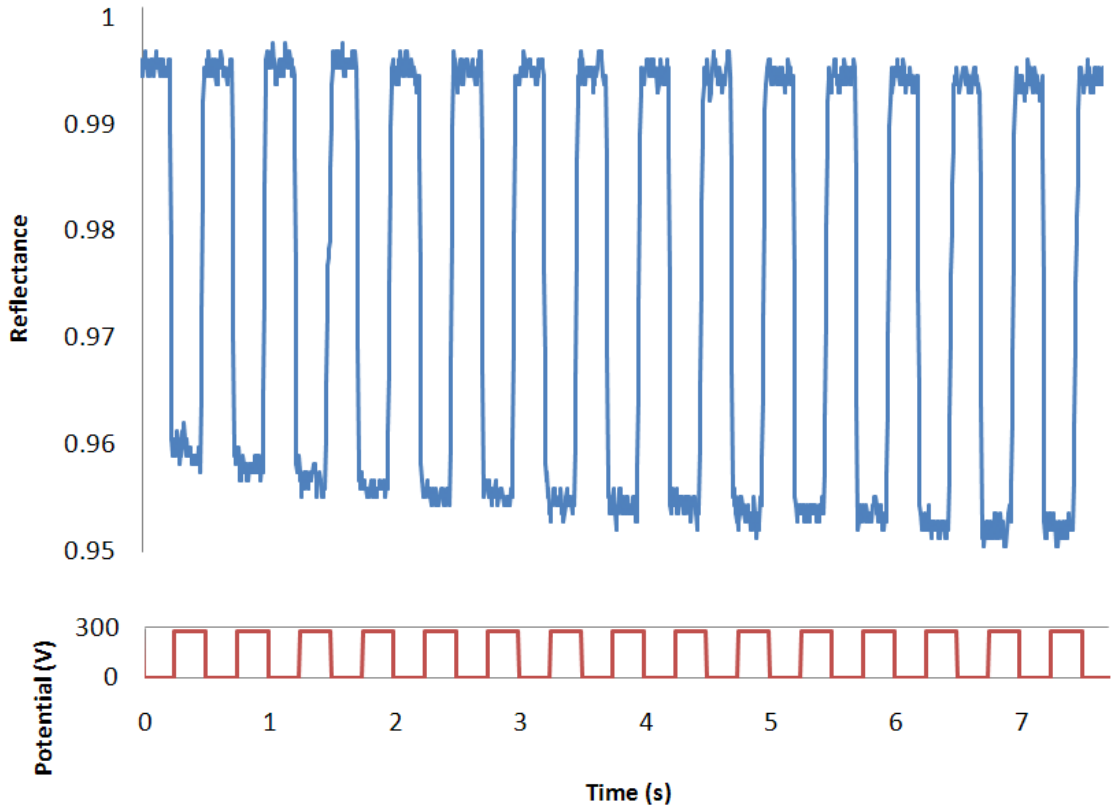

Figure 5.7: Reflectance response of FTIR device to multiple cycles of applied potential. The red curve on the bottom is the applied electrical potential and the blue curve on top is the corresponding measured reflectance.

5.5 Time response

A closer look at the optical response of the system was studied using a 20 kHz data sampling rate. In Figure 5.8, a single cycle is shown of the optical response to an applied potential. As the sampling rate is an order of magnitude greater than the applied signal frequency, the actual applied potential is measured during high frequency data sampling. Plotted in Figure 5.8 are the amplitude of the applied potential, between 0 and 280V, and the normalized intensity of the reflected light. The dotted black lines are for illustrative purposes only.

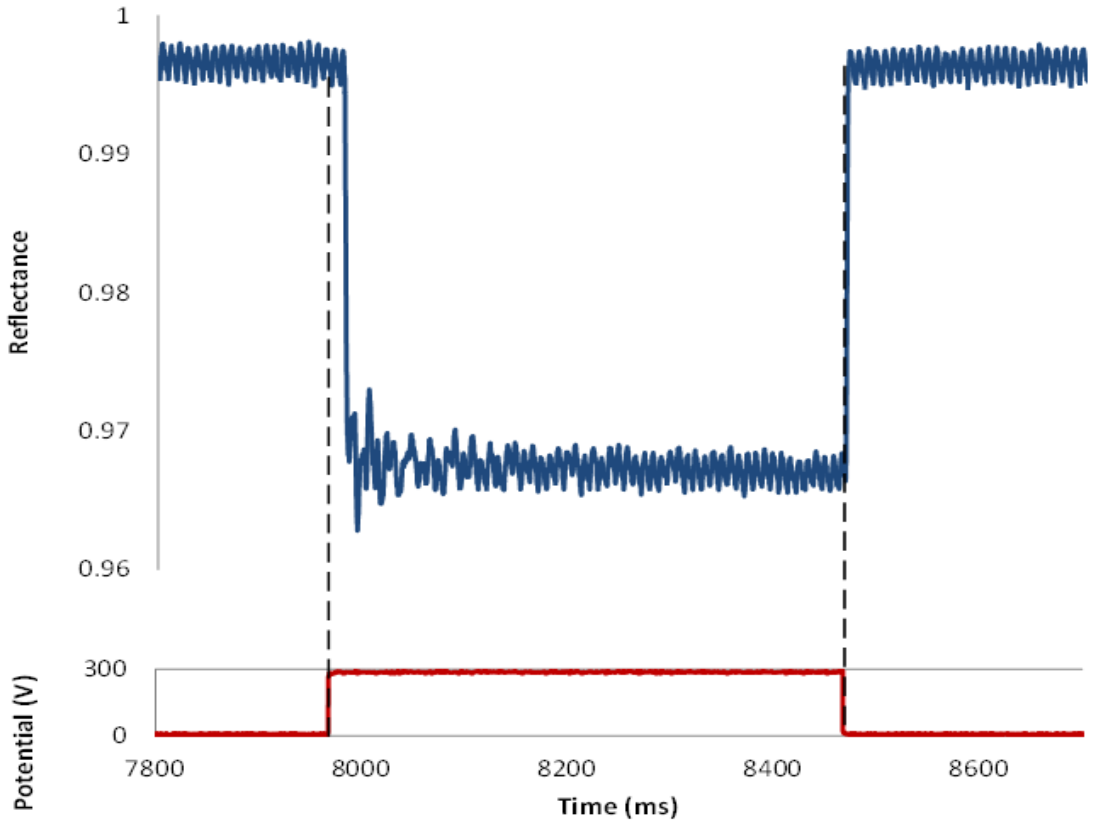

Figure 5.8: Optical response of FTIR device to applied potential with 20 kHz data sampling. The red curve on the bottom is the applied electrical potential and the blue curve on top is the corresponding measured optical reflectance.

Photographs were taken concurrently during the data acquisition and show the movement of the water drop in response to the applied potential. The photographs were taken through a microscope and show a side view of the device similar to the view depicted in the schematic drawing in Figure 5.2.

In Figure 5.9(a), no electrical potential was applied and the water drop was positioned on top of the trench structure and out of optical contact of the transparent superhydrophobic surface. Below the water drop, the reflection of the drop on the surface of the PMMA film can be seen. In Figure 5.9(b), a potential was applied between the water drop and the underlying ITO electrode. The water drop deformed and visibly made optical contact with the PMMA

surface as the drop and its reflection touched. In Figure 5.9(c), the applied potential was once again zero and the water drop returned to its original curvature, having overcome the force of adhesion between it and the PMMA surface.

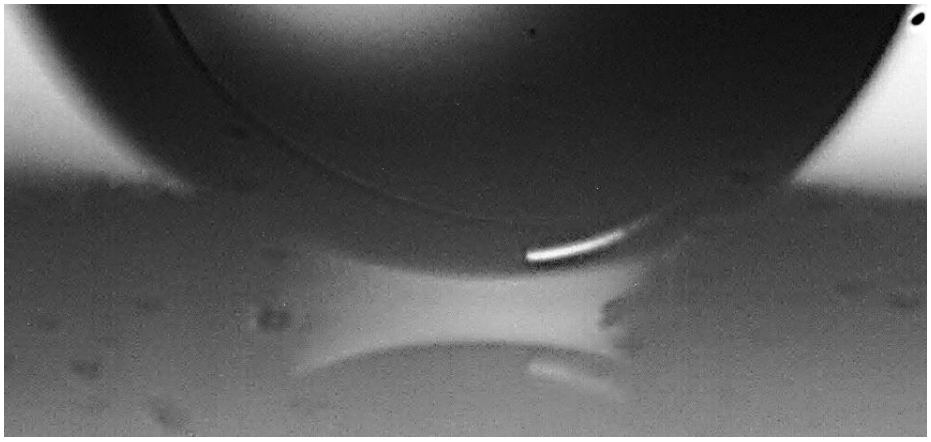

(a)

(b)

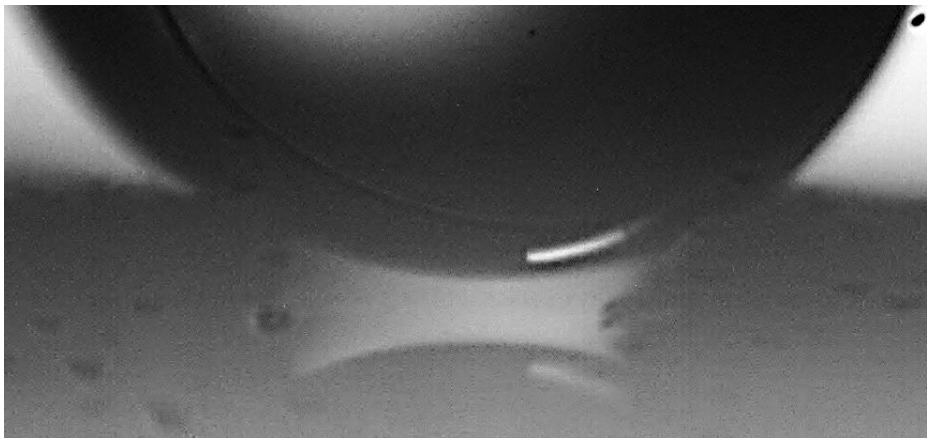

(c)

Figure 5.9: Images taken during data acquisition a) before applied potential b) during applied potential and c) after applied potential is released

The optical reflected intensity immediately after the applied potential changes from 0V to 280 V and from 280 V to 0 V in Figure 5.8 reveals some interesting insights. Figure 5.10 shows the same data as in Figure 5.8, zoomed in to when the electrical potential difference changes from 0 V to 280 V such that the horizontal time axis is stretched out. The data shows a 10 ms delay between the application of the electrical potential and the beginning of the optical response of the system. This is due to the time it takes for the water to deform into the trench structure before making optical contact with the PMMA surface. This time delay can be drastically reduced by decreasing the size of the large trench structures. The trenches in this experiment are 150 μm high and this size was chosen for ease of study and fabrication. The trenches can be made as small as the size of the evanescent wave region, which is on the order of 1μm, to reduce the optical response speed.

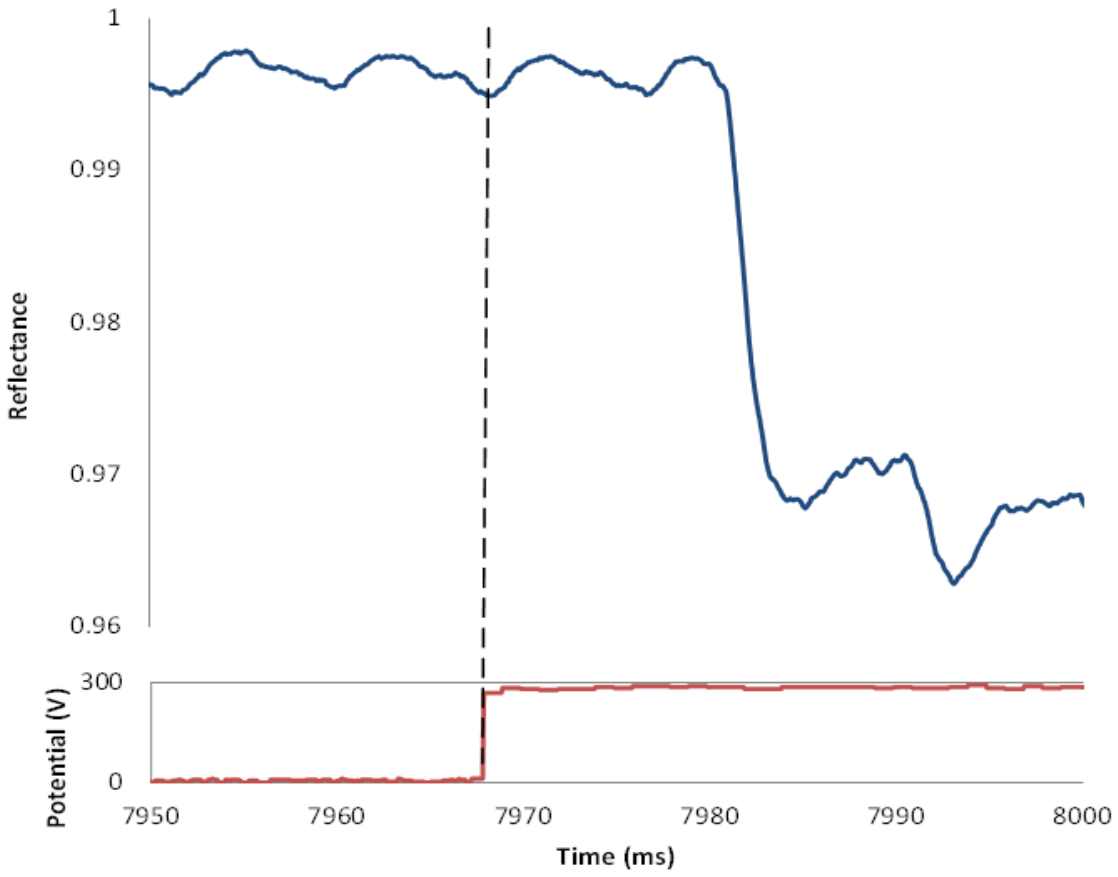

Figure 5.10: Optical reflectance when applied potential is increased from 0V to 280V. The red curve on the bottom is the applied electrical potential and the blue curve on top is the corresponding measured optical reflectance.

It is illustrative to discuss how the applied voltage scales as the dimensions of the FTIR device decreases. For simplicity's sake, it will be assumed that the height of the trench structures and the thickness of the PMMA dielectric layer scale together linearly and the size of the water drop stays constant. As the trench height and dielectric thickness are reduced, the pressure difference that the water drop must undergo to make optical contact with the transparent surface should remain the same, as this is determined solely by the energy of adhesion between the water and superhydrophobic PMMA surface. Thus, the width of the trench does not scale linearly with the trench height but rather is calculated by Equation (16) such that the deformation the water drop must undergo to make optical contact with the PMMA surface remains constant. As the pressure applied to the water drop remains the

same, the applied voltage is roughly linearly proportional to the trench height and dielectric thickness according to Equation (11).

As an example, the FTIR device tested in these experiments have a 100 μm thick PMMA layer and trench dimensions of 150 μm high and 600 μm wide. These devices require an applied voltage of 280 V amplitude. If the height of the trench structures and the thickness of the dielectric PMMA layer were to be reduced by a factor of ten, then the width of the trench can be calculated according to Equation (16) to be 210 μm. Since the distance between the water and bottom electrode are reduced by a factor of ten and the required pressure applied to the water drop remains the same, the applied voltage is reduced by a factor of ten according to Equation (11). Thus, for a device with 15 μm high, 210 μm wide trenches, and a PMMA thickness of 10 μm, the required applied electrical potential would be 28 V. If the device were to be used in an optical display, then the width of the trench could be thought of as the pixel size. For comparison, a 12 inch diagonal display with a resolution of 1280x800 pixels has a pixel size of approximately 215 μm, so 210 μm is a reasonable pixel size for an optical display.

Figure 5.11 shows the reflected intensity when the applied potential is reduced from 280V to 0V across the FTIR device. In it, the data shows a 1.5 ms time delay between the time the electrical potential is removed and when the reflectance returns to its original value.

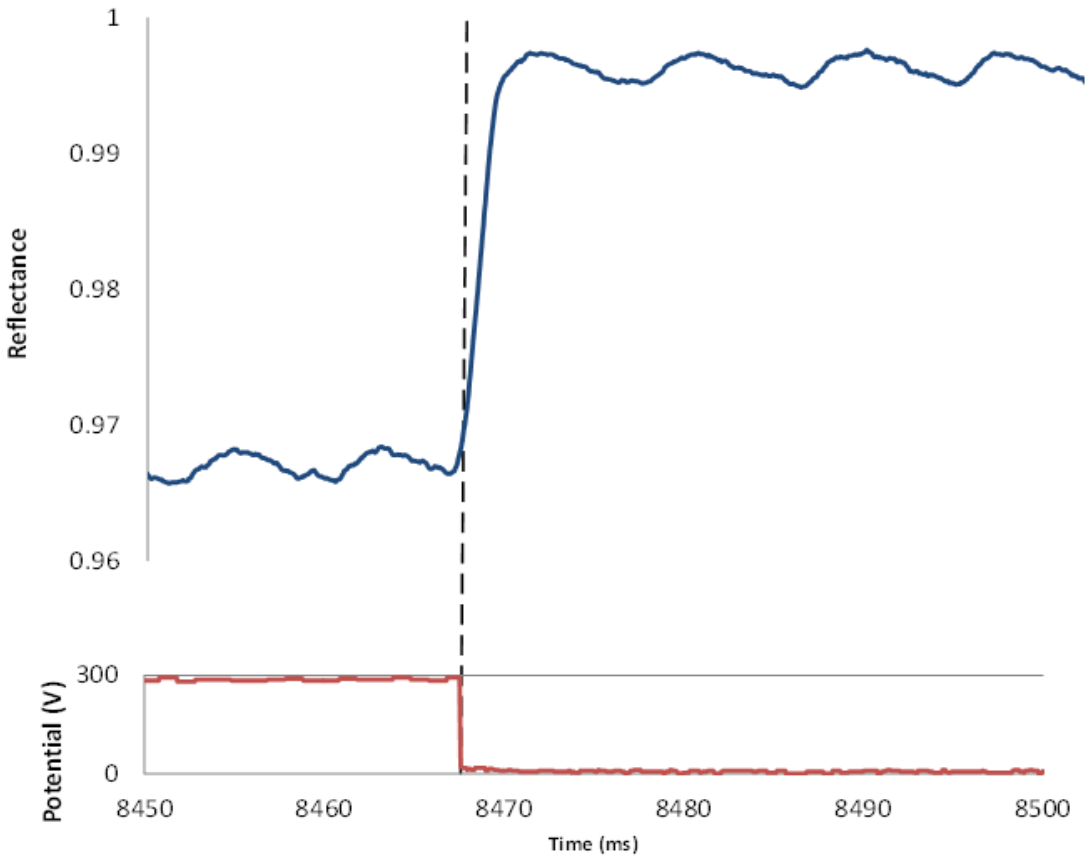

Figure 5.11: Optical reflectance when applied potential is reduced from 280V to 0V. The red curve on the bottom is the applied electrical potential and the blue curve on top is the corresponding measured optical reflectance.

The FTIR device presented demonstrates an optical response time between 1 and 10 ms, and repeatability over multiple cycles. The properties of this device suggest that this technique is practical in the application of electrically controlled reflective image displays.

6 CONCLUSION

An important aim of this study was to investigate the wetting behavior of structured surfaces and to fabricate superhydrophobic surfaces with high optical transparency. The knowledge and expertise gained from these activities were then applied to the fabrication and demonstration of a device that reversibly changes the reflectance at a surface by electrically controlling frustration of total internal reflection.

A novel visualization technique involving neutrally buoyant, immiscible liquids was used to visualize the wetting behaviors of micro and nano-structured surfaces. This technique clearly showed the fundamental importance of the intrinsic contact angle to the design and behavior of superhydrophobic surfaces. This technique is useful not only as a method of visualizing the effect of new surface geometries but also as an educational tool to clearly communicate understanding of superhydrophobic surfaces and wetting phenomena. This is not a trivial application, as there are several recent publications on the widely held misconceptions of superhydrophobicity, with one lamenting that "…the teaching of surface science over the last century has led generations of students and scientists to a misunderstanding of the wetting of solids by liquids" (4).

In order to fabricate superhydrophobic surfaces for this study, two techniques for creating transparent porous films and two techniques for applying hydrophobic coatings to surfaces were explored. A fabrication technique for producing transparent superhydrophobic surfaces by plasma etch of PMMA and Teflon® AF coating was optimized. Resulting samples were shown to be superhydrophobic, with contact angles of 159±1º and contact angle hysteresis of 6±2º. A calculation was developed to predict the adhesion force of these surfaces from contact angle measurements. The roughness of these surface geometries was found to be small enough to allow significant intensity of light to be frustrated by water on its surface. The optical properties of these surfaces were modeled using the GSolver© software, and experimentally confirmed. Future research into the further optimization of the transparent PMMA superhydrophobic surface would be beneficial, to decrease roughness feature sizes without compromising superhydrophobic robustness. This would allow water to travel closer

into the evanescent wave region, resulting in a higher change in reflectance by frustration of TIR.

A new technique to electrically modulate the reflectance at an interface was demonstrated with the FTIR device. The FTIR device consisted of water resting on a dual-scaled superhydrophobic structure. Application of electrical potential resulted in the deformation of the water drop, causing it to come into optical contact with the transparent interface. Release of the electrical potential caused the water to return to its original shape, breaking contact with the low adhesion, transparent surface. AC potentials were required to minimize charge leakage due to the electrical conductance of air. Due to the high electrostatic pressure applied to the water when in optical contact with the superhydrophobic PMMA surface, a capacitor was placed in series with the device to provide passive feedback. This reduced the applied voltage and therefore, electrostatic pressure when water came into optical contact with the PMMA surface. It was determined experimentally at an angle of incidence 1.5º from critical angle that an application of 198V RMS caused a reversible reflectance change of 4% at the device surface. The time delay between applied potential and the change in reflectance was about 10 ms. During this time, the water deformed under electrostatic pressure and travelled the distance of the air gap between it and the PMMA surface. The time delay between the removal of the electrical potential and complete change in reflectance was about 1.5 ms.

The FTIR device shows promise as a potential reflective-based display, in part due to its high speed optical response. Future work into scaling down the size of the large trench structures would be beneficial. Current trench sizes are 150 μm high, simply for ease of fabrication. If the large structures were on the micrometer size-scale, time delay between the application of electrical potential and the optical response would be greatly reduced. The smaller structures would also result in lower operating voltages, as the voltage scales with the inverse of distance at a fixed electrostatic pressure.

In summary, this thesis has presented a new technique for electrically modulating the frustration of total internal reflection. The results demonstrate the potential of this technique and suggest further research is warranted. Although this thesis has focused on the control and study of reflectance, other potential applications could exploit the transmitted, frustrated

light. This could be used, for example, in variable beam splitting or signal switching applications.

REFERENCES

[1]Neinhuis, C., Barthlott, W., "Characterization and Distribution of Water-Repellent, Self-cleaning Plant Surfaces". *Annals of Botany*, Vol. 79(6), 667-677, 1997

[2]Roach, P.L., et al., "Progress in Superhydrophobic Surface Development". *Soft Matter*, Vol. 4(2), 224-240, 2008

[3]Li, X., et al., "What Do We Need for a Superhydrophobic Surface? A Review on the recent Progress in the Preparation of Superhydrophobic Surfaces". *Chem Soc Review*, Vol. 36, 1350-1368, 2007

[4]Gao, L., McCarthy T.J., "An Attempt to Correct the Faulty Intuition Perpetuated by the Wenzel and Cassie 'Laws'". *Langmuir*, Vol. 25(13), 7249-7255, 2009

[5]Gao, L., McCarthy T.J., "Wetting 101". *Langmuir*, Vol. 25(24), 14105-14115, 2009

[6]Kroeker, K.L., "Electronic Paper's Next Chapter", *Communications of the ACM*, Vol. 52(11), 15-17, 2009

[7]Pedrotti F.L., et al., *Introduction to Optics* (3rd ed.), p 249, Pearson Prentice Hall, Upper Saddle River NJ, 2007

[8]Hecht, E. *Optics* (4th ed.), pp. 126-127, Addison Wesley, San Francisco CA, 2002

[9] Teflon® AF, Product Identification Number 400S2-100-1, manufactured by DuPont Fluoropolymer Solutions, Wilmington, DE, 19880-0705, USA

[10]Tsio S., et al., "Surface Functionalization of Porous Nanostructured Metal Oxide Thin Films Fabricated by Glancing Angle Deposition". *Chemistry of Materials*, Vol. 18(22), 5260-5266, 2006

[11]Vourdas, N., et al., "Nanotextured Super-Hydrophobic Transparent Poly(methyl methacrylate) Surfaces Using High-Density Plasma Processing". *Nanotechnology*, Vol. 18(12), 125304, 2007

[12]Ibid 7, p. 505

[13] Wenzel, R.N., "Resistance of Solid Surfaces to Wetting by Water". *Industrial and Engineering Chemistry*, Vol. 28(8), 988-994, 1936

[14] Cassie, A.B.D., Baxter, S., "Wettability of Porous Surfaces". *Trans Faraday Soc.*, Vol. 40, 546-551, 1944

[15] Ibid 3

[16] Ibid 13

[17] Ibid 14

[18] Ahuja A., et al., "Nanonails: A Simple Geometrical Approach to Electrically Tunable Superlyophobic Surfaces". *Langmuir*, Vol. 24(1), 9-14, 2008

[19] Park Y., et al., "Superhydrophobic Cylindrical Nanoshell Array". *Langmuir*, Vol. 26(11), 7661-7664, 2010

[20] Ibid 1

[21] Ibid 4

[22] Ibid 4

[23] Ibid 5

[24] Gao, L., McCarthy, T., "How Wenzel and Cassie Were Wrong", *Langmuir*, Vol. 23(7), 3762-3765, 2007

[25] Gao, L., McCarthy, T., "Reply to 'Comment on How wenzel and Cassie Were Wrong by Gao and McCarthy'". *Langmuir*, Vol 23(26), 13243, 2007

[26] Ibid 24

[27] Kusumaatmaja H., et al., "Anisotropic Drop Morphologies on Corrugated Surfaces". *Langmuir*, Vol. 24(18), 7299-7308, 2008

[28] Gu Z.Z., "Structural Color and the Lotus Effect". *Angewandte Chemie*, Vol. 42, 894-897, 2003

[29] Ibid 24

[30] Brakke, K., "The Surface Evolver". *Experimental Mathematics*, Vol. 1(2), 141-165, 1992

[31] Chen, Y., et al., "Anisotropy in the Wetting of Rough Surfaces". *J Colloid and Interface Science*, Vol. 281(2) 458-464, 2005

[32] Dorrer, C., Ruhe, J., "Contact Line Shape on Ultrahydrophobic Post Surfaces", *Langmuir*, Vol. 23(6), 3179-3183, 2007

[33] Anantharaju, N., et al., "Effect of Three-Phase Contact Line Topology on Dynamic Contact". *Langmuir*, Vol 23(23), 11673-11676, 2007

[34] Gelest Inc., "Hydrophobicity, Hydrophilicity and Silane Surface Modification". 2006

[35] Fluorinert™ FC-75 Electronic Liquid, Product Identification Number 98-021103996-3, manufactured by 3M Company, St. Paul, MN, 55144-1000, USA

[36] http://www.ece.ualberta.ca/~glad/glad.html.

[37] Ibid 36

[38] Ibid 36

[39] Ibid 10

[40] http://www.plasmatechnology.com/cleaning.php

[41] Zimin, S.P., et al., "Micromasking effect and nanostructure self-formation on the surface of lead chalcogenide epitaxial films on Si substrates during argon plasma treatment". *J Phys D: App.l Phys.*, Vol. 42, 165205-165211, 2009

[42] Ibid 11

[43] Ibid 11

[44] Type A Immersion Oil, Cat #: 16482, manufactured by Cargille Labs, Cedar Grove, NJ, 07009, USA

[45] High-Sensitivity Light-to-Voltage Converter, Product Identification Number TSL 257, manufactured by Texas Advanced Optoelectronic Solutions Inc., TX, 75074

[46] Grossweiner, L.I., *The Science of Phototherapy, An Introduction,* P. 47, Springer, Dordrecht, 2005

[47] Angle Platform tilt stage, Model Number MXT, manufactured by Siskiyou Corporation, Grants Pass, OR, 97526, USA

[48] GSolver© diffraction grating analysis software, a product of Grating Solver Development Company, Allen, TX, 75013, USA

[49] http://www.gsolver.com/

[50] Scotch® Magic™ Tape brand tape, Cat. 810-NA, manufactured by 3M Company, St. Paul, MN, 55144-1000, USA

[51] WX2100™ superhydrophobic coating, manufactured by Cytonix Corporation, Beltsville, MD, 20705, USA

[52]Li, F., Mugele, F., "How to Make Sticky Surfaces Slippery: Contact Angle Hysteresis in Electrowetting with Alternating Voltage", *Applied Physics Letters,* Vol. 92(24), 2008

[53] Seeger, J.I., Crary, S.B., "Stabilization of Electrostatically Actuated Mechanical Devices". *Proc Transducers '97 Chicago*, Vol. 2, 1133-1136, 1997

[54] Ibid 53

APPENDIX A: STANDARD OPERATING PROCEDURE FOR SILANE COATING

This is the recipe used to coat surfaces with a monolayer of octadecyltrimethoxysilane.

1) Clean surface using the following process.
    a. Mix deionized water and ammonium hydroxide in a ratio of 5:1 by volume
    b. Heat mixture to 65°C-70°C
    c. Add 1 part by volume of hydrogen peroxide to mixture
    d. Place samples to be cleaned into solution for 30 minutes
    e. Remove samples from solution
2) Rinse samples with deionized water
3) Dry samples with nitrogen gun
4) Prepare solution of 1% by volume octadecyltrimethoxysilane in toluene
5) Add a small drop of acetic acid to catalyze reaction
6) Place samples into toluene solution and seal container to avoid evaporation
7) Wait for 72 hours
8) Take samples out and rinse with toluene
9) Bake sample at 100°C for 24 hours
10) Store sample under vacuum until ready to use

APPENDIX B: GLANCING ANGLE DEPOSITION SETUP

The GLAD films made for this experiment were vertical post GLAD films. As the controls necessary to make vertical post GLAD films are relatively simple compared to other geometries, such as chevrons, some simplifications were made in the Glancing Angle Deposition setup used.

The substrate is mounted on a vertical sample holder, which is attached to a rod that is free to rotate. To the opposite end of the rod, a magnet is attached. This assembly was mounted inside the vacuum chamber of an electron beam evaporator, and above the source material. The deposition angle was controlled by changing the horizontal position of the sample with respect to the source material (Figure B.1).

The substrate's rotation was controlled by a second magnet attached to a motor outside the vacuum chamber. As the second magnet rotates, it couples with the magnet inside the chamber, rotating the rod and sample (Figure B.2). In this way, a simple GLAD setup for vertical post GLAD films was made without the need for electrical or mechanical feedthroughs into the vacuum chamber.

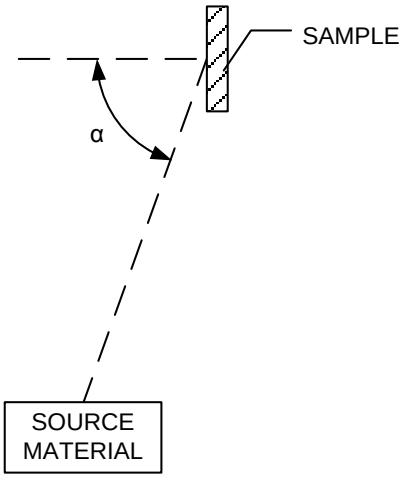

Figure B.1: Deposition angle between the source and substrate during Glancing Angle Deposition

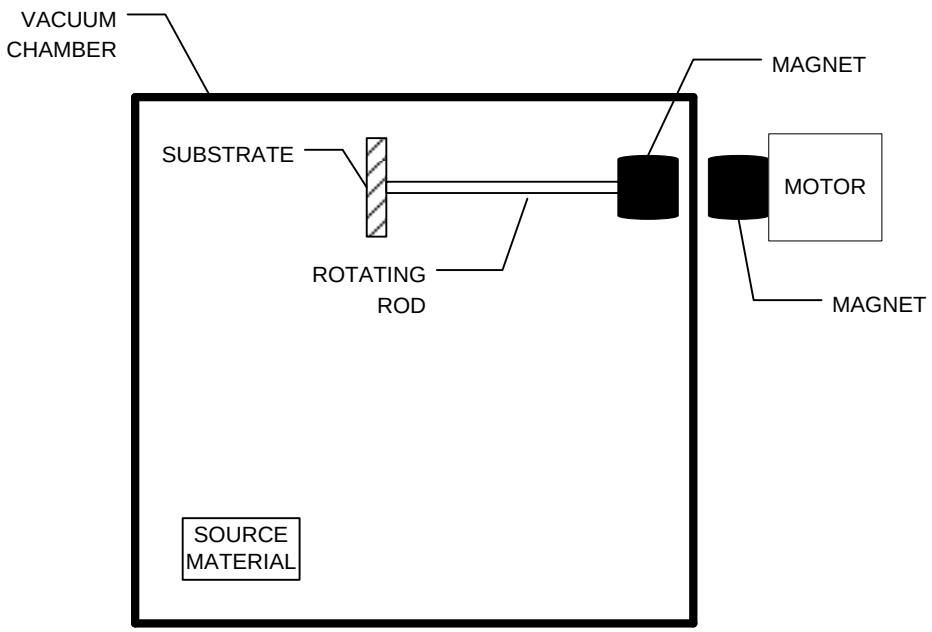

Figure B.2: Experimental setup at the University of British Columbia for deposition of GLAD films

APPENDIX C: STANDARD OPERATING PROCEDURE FOR FABRICATION OF SUPERHYDROPHOBIC PMMA SURFACES VIA OXYGEN PLASMA ETCH

Oxygen Plasma Etching

Oxygen plasma etching was done in a SENTECH Etchlab 200 and its relevant properties are listed in Appendix C.

1) Clean ITO on glass slide with methanol and water in ultrasonic bath. Each slide has dimensions of approximately 25mm x 35mm in area and 1.1mm thick.
2) Measure out 0.30 g of Microchem 905PMMA A11 PMMA in anisole
3) Apply PMMA in anisole onto ITO surface using a pipette
4) Allow PMMA in anisole to cure overnight at room temperature on ITO on glass slide. The resultant PMMA layer should be approximately 100 μm thick.
5) Etch two PMMA samples at a time in reactive ion etcher using the following parameters:
    a. Oxygen flow 40 sccm
    b. Pressure 50 mT
    c. Etch time 110 seconds
    d. Power 600 W
6) Spin coat Teflon® AF onto etched PMMA using the following parameters:
    a. Mix Teflon® AF 400S2-1-1 with FC-75 in ratio of 1:4 by weight
    b. Spin coat at 500RPM for 18 seconds
    c. Cure sample for 5 minutes at 100ºC
    d. Repeat for a total of 4 coats
7) Store in desiccator under vacuum until use

Oxygen Plasma Clean

It was found that the superhydrophobic samples produced with this method were most robust if the samples were Teflon® AF-coated immediately after plasma etching. If samples are to

be Teflon® AF-coated sometime after the etch step, they were stored under vacuum. A low power plasma clean in a TRION RIE/PECVD was then performed before Teflon® AF-coating.

The parameters for the plasma clean are:

a) Pressure = 500 mT
b) Power = 50 W
c) Temperature = 20°C
d) Time = 10 seconds
e) Oxygen Flow = 50 sccm

APPENDIX D: CALCULATION OF ADHESION FORCE BETWEEN WATER AND A SURFACE

This calculation finds the force necessary for a water drop to separate from a surface. In this particular calculation, the water drop is in contact with two parallel solid surfaces as depicted in Figure D.1. This was to simulate the experimental setup used to measure the adhesion force between water and superhydrophobic surfaces. Cylindrical symmetry is assumed. This calculation also assumes that the contact angles between the water and the two solid surfaces remains constant as the spacing *d* between the two surfaces increases. However, in reality, contact line pinning will have an effect on the contact angle as the contact line moves.

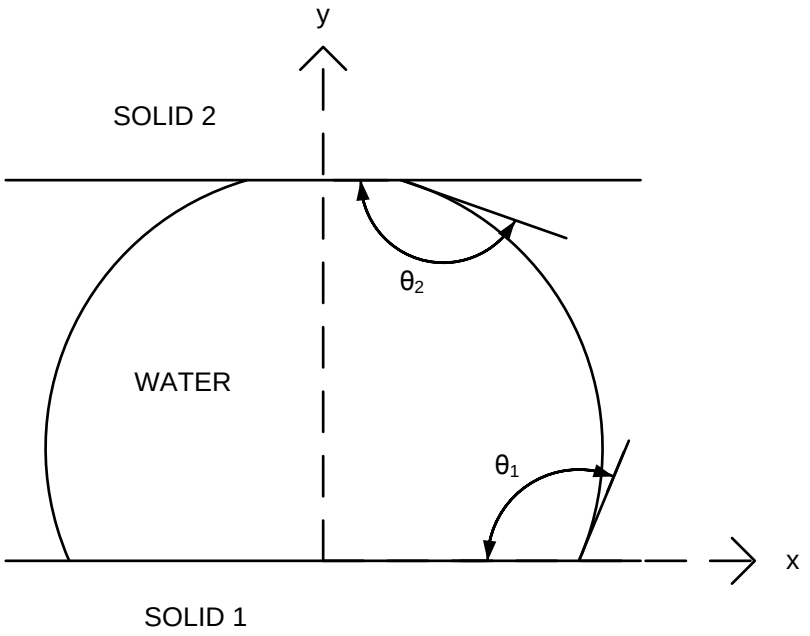

Figure D.1: Water drop between two parallel surfaces

The calculation finds a solution to the shape of the drop by following these steps:

1) A water drop is in contact with two solid surfaces spaced *d* distance apart and makes a cylindrically symmetric shape between the two surfaces

2) The drop is approximated as *N* equally spaced horizontal slices, or thin cylinders, as shown in Figure D.2. The problem simplifies to two dimensions due to cylindrical symmetry.

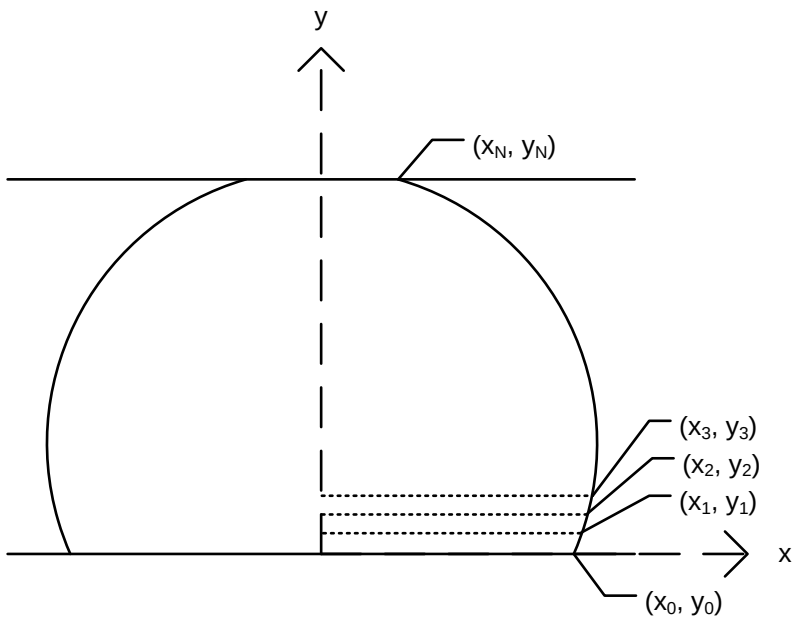

Figure D.2 The water drop was approximated as equally spaced slices for this calculation

3) The shape of the drop is represented as a set of coordinates, *(x_0, y_0), (x_1 y_1)… (x_n, y_n)*. As each horizontal slice is equally space,

$$y_n = y_{n-1} + \Delta y$$

where

$$\Delta y = d/N$$

4) x_n can be found iteratively by:

$$x_n = x_{n-1} + \Delta y x'_{n-1}$$

5) x'_n can also be found iteratively:

$$x'_n = x'_{n-1} + \Delta y x''_{n-1}$$

6) x''_n is found from the curvature of the water from the relationship:

$$R_{in} = \frac{(1 + x'^2)^{3/2}}{x''}$$

where R_{in} is the radius of curvature in the x-y plane

7) The pressure throughout the water drop is constant and the radius of curvature R_{in} is found from the relationship:

$$\Delta P = 1/R_{in} + 1/R_{out}$$

8) R_{out} is the radius of curvature perpendicular to R_{in} and tangent to the drop surface and can be determined by geometric considerations. R_{out} can be visualized as the curvature of a cone as illustrated in Figure D.3. R_{out} of the cone in Figure D.3(b) is equal to the R_{out} of the point on the drop where the slope, *dx/dy*, is equal to the slope of the side of the cone. The curvature, R_{out}, is found to be:

$$R_{out} = \frac{x(y)}{\cos(\pi - \tan^{-1} x'(y))}$$

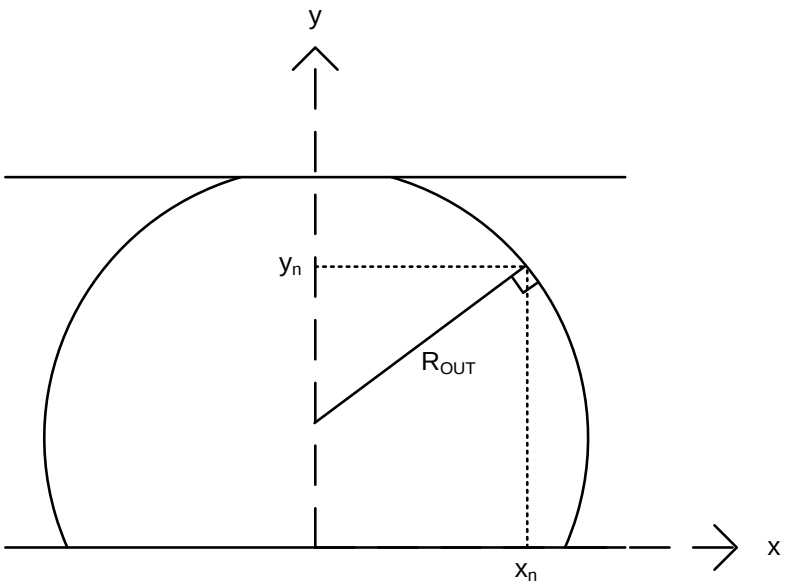

(a)

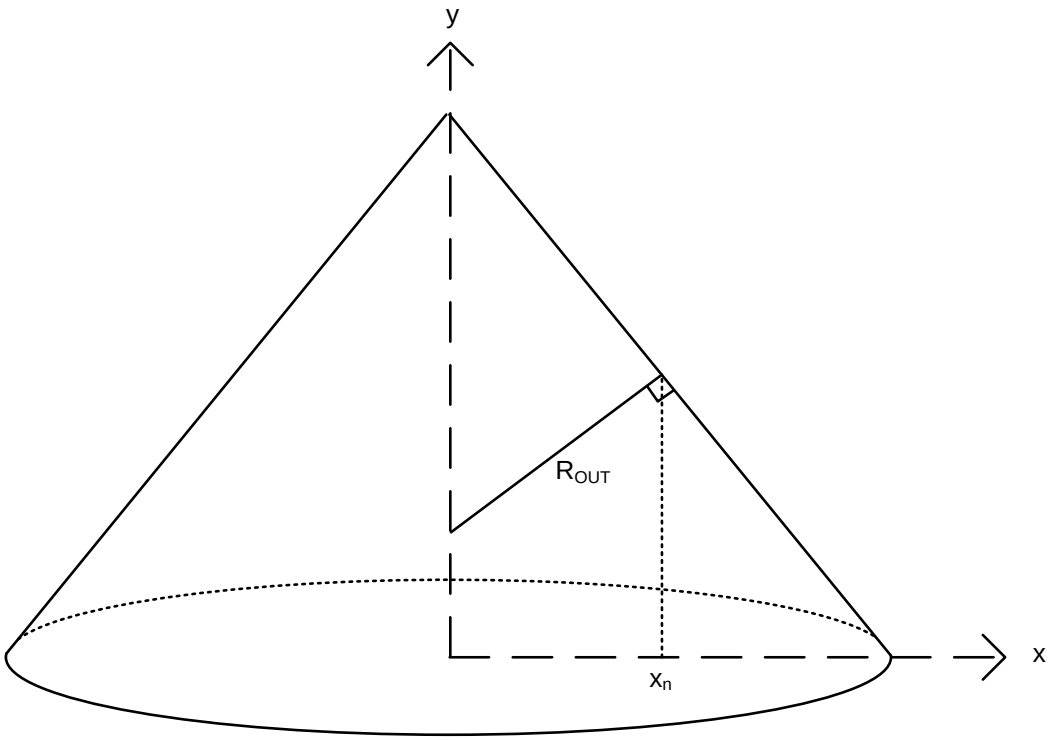

(b)

Figure D.3: a) The radius of curvature out of the plane of the drop shape b) The radius of curvature out of the plane can be calculated from that of a cone with the same slope

9) Because contact angles are constant between the water and the two surfaces, x_0' and x_n' are given. The total volume of the drop is also constant

10) Given these relationships, we now have enough information to numerically solve for the shape of the water.

11) Specifically, this was done using Solver in Microsoft Excel and was found by making d and θ_1 constants, allowing Solver to adjust x_0 and pressure until a target volume and θ_2 was iteratively reached.

12) Once a solution was been found, the areas of each interface was calculated. This was then converted to the energies associated with each interface

13) The spacing between the two surfaces is then increased by an amount Δd and the calculation is repeated for the new spacing

14) Applied force is calculated by finding the total change in energy as the spacing d is changed, and dividing by the change in spacing distance

15) This calculation is repeated for increasing spacings d until a maximum force is found. At this point, the water drop snaps off the surface of higher contact angle. The maximum force calculated is the force necessary to separate the water from the surface of higher contact angle, and thus, is the force of adhesion between the water and the surface.

APPENDIX E: MATERIALS LIST

Materials and key equipment used in this research are listed in the following table, along with the supplier and important features.

Table E.1: Materials List

Material	**Supplier**	**Important properties**
Indium Tin Oxide coated float glass	Delta Technologies Limited 13960 North 47th St Stillwater, MN 55082-1234 USA	Product Number: CF-90IN-S115 R_S = 70-100Ω
Type A Immersion Oil	Cargille Laboratories, Inc. Cedar Grove, NJ 07009 USA	Index of Refraction: 1.515
Teflon® AF 400S2-100-1	DuPont Fluoropolymer Solutions Wilmington, DE 19880-0705 USA	1% by weight Teflon® AF solid in fluorinert solution Contact angle: 110°
Fluorinert Solvent	3M Company St. Paul, MN 55144-1000 USA	FC-75 Product Identification Number 98-0211-3996-3 Boiling point = 102°C
Digital Camera	Nikon Inc. Melville, NY 11747-3064 USA	Coolpix 995 3.34 Megapixel Resolution
Silicon Camera	Silicon Imaging 25 Covington Court Niskayuna, NY 12309 USA	Model number: SI1920RGB-CL Mounts to trinocular microscope

Material	**Supplier**	**Important properties**
Mineral Oil, Light	Fisher Scientific Company 112 Colonnade Road Ottawa, Ontario K2E 7L6 Canada	CAS #: 8042-47-5 Density = 0.84g/cm^3
Superhydrophobic Coating	Cytonix 8000 Virginia Manor Road Beltsville, MD 20705 USA	Product name: WX2100^{TM} Contact Angle 150°
RIE/PECVD	TRION Technologies 2131 Sunnydale Blvd. Clearwater, FL 33765 USA	ORION Model Load locked PECVD Electrode diameter: 200mm
PMMA in solvent	Microchem Corp. Newton, MA 02464 USA	PMMA 950 A11 11% by weight PMMA in anisole Index of refraction: 1.49-1.52
Plasma Etcher	SENTECH Instruments GmbH 12489 Berlin, Germany	SENTECH Etchlab 200 Reactor diameter: 298mm Electrode diameter: 215mm
Octadecyltrimethoxysilane	Gelest Inc. Morrisville, PA 19067 USA	Product number: SiO6645.0